J. Fluid Mech. (2010), *vol.* 648, *pp.* 405–434. © Cambridge University Press 2010
doi:10.1017/S0022112009993193

Internal gravity waves generated by convective plumes

JOSEPH K. ANSONG[1] AND BRUCE R. SUTHERLAND[2]†

[1]Department of Mathematical and Statistical Sciences, University of Alberta, Edmonton, AB, T6G 2G1, Canada

[2]Departments of Physics and of Earth and Atmospheric Sciences, University of Alberta, Edmonton, AB, T6G 2G7, Canada

(Received 9 July 2009; revised 30 October 2009; accepted 1 November 2009)

We present experimental results of the generation of internal gravity waves by a turbulent buoyant plume impinging upon the interface between a uniform density layer of fluid and a linearly stratified layer. The wave field is observed and its properties are measured non-intrusively using axisymmetric Schlieren. In particular, we determine the fraction of the energy flux associated with the plume at the neutral buoyancy level that is extracted by the waves. On average, this was found to be approximately 4 %. Within the limits of the experimental parameters, the maximum vertical displacement amplitude of waves were found to depend linearly upon the maximum penetration height of the plume beyond the neutral level. The frequency of the waves was found to lie in a narrow range relative to the buoyancy frequency. The results are used to interpret the generation of waves in the atmosphere by convective storms impinging upon the tropopause via the mechanical oscillator effect.

1. Introduction

Internal gravity waves have been studied over the years in part because of their affect upon the circulation patterns in the ocean and atmosphere. For example, the momentum transported by convectively generated gravity waves in the tropics have been suggested to drive the quasi-biennial oscillation (Dunkerton 1997). The contribution of gravity waves in general to the dynamics of the quasi-biennial oscillation has been suggested in earlier studies (Lindzen & Holton 1968; Holton & Lindzen 1972). The waves are also known to affect the global momentum budget in the middle and upper atmosphere as well as in the troposphere through wave drag. Their inclusion in general circulation models (GCMs) is necessary for a greater understanding of circulations in the atmosphere and for that matter accurate predictions of global weather patterns (McLandress 1998). By necessity, GCMs use coarse grids with long time steps and so to include the effects of relatively small and fast internal gravity waves in their models, researchers attempt to parameterize their effects. Besides their influence on the large-scale flows, gravity waves above convection have also been suggested to cause mixing and cirrus cloud initiation when they break (Moustaoui, Joseph & Teitelbaum 2004; Wang 2004; Lane & Sharman 2006).

† Email address for correspondence: bruce.sutherland@ualberta.ca

Various sources of gravity wave generation have long been identified. These include flow over topography, geostrophic adjustment and deep convection (Fovell, Durran & Holton 1992). It is now appreciated that the last of these is also significant, particularly in the tropics, but the detailed mechanism for wave generation by convection is not well understood.

Three main ways of generating internal gravity waves by deep convection have been identified in the literature. They include the mechanical oscillator effect (Pierce & Coroniti 1966; Clark, Hauf & Kuettner 1986; Fovell *et al.* 1992), the obstacle effect (Clark *et al.* 1986) and the deep heating effect (Pandya & Alexander 1999; Alexander & Barnet 2007). In the mechanical oscillator effect, the vertical oscillations of updrafts and downdrafts are believed to excite internal gravity waves in the stable layer above the troposphere similar to the way in which the waves may be generated by an oscillating rigid body. In the obstacle effect, updrafts act as an obstacle to a mean horizontal flow at the cloud tops and this excites gravity waves in the stable layer above. To avoid any confusion with internal gravity wave generation by flow over topography, this mechanism has also been called 'quasi-stationary forcing' (Fovell *et al.* 1992). In the deep heating effect, thermal forcing by latent heat release within a convective system acts as gravity wave source (Pandya & Alexander 1999; Alexander & Barnet 2007). The initial studies of Clark *et al.* (1986) concluded that the obstacle effect was the most important wave generation mechanism. However, the studies by Fovell *et al.* (1992) and later Kumar (2007) show that parcel oscillations within convective updrafts and downdrafts are also responsible for generating the gravity waves. An extensive review by Fritts & Alexander (2003) concluded that all three mechanisms may be important with one mechanism or another serving to explain a set of observations depending upon the environmental conditions.

In a recent study by Kumar (2007), it was pointed out that among convective generation processes, the least understood is the mechanical oscillator effect. Using VHF radar measurements and wavelet analyses, Kumar (2007) carried out a study that showed the observational evidence of the role of the mechanical oscillator effect. The study also mentioned the lack of adequate information to parameterize the full spectrum of convective gravity waves from the various numerical modelling and observational studies and suggested a collaboration among theories, models and observations.

In this paper, we report upon laboratory experiments designed to isolate the dynamics of the mechanical oscillator effect acting within a convective storm. Specifically, we examine properties of axisymmetric waves emanating from a plume impinging upon a stratified fluid. The waves are visualized and their characteristics and amplitudes are measured using an axisymmetric synthetic Schlieren method that measures the amplitudes of axisymmetric disturbances (Onu, Flynn & Sutherland 2003).

Although the experiments presented in this study are performed with application to the atmosphere as the focus, the results may also be applied to oceanic deep convection. A combination of thermodynamic effects such as rapid cooling, evaporation and freezing may cause surface waters to become denser than deep waters, thereby causing parcels of water to sink with entrainment of ambient fluid. These convective plumes have been observed to mix vigorously with their surroundings as they sink with velocities of 2–10 cm s^{-1}, with vertical scales of 1–2 km, and with horizontal scales of the order of 1 km and occur on time scales of several hours to days (Paluszkiewcz & Garwood 1994). A study in the Mediterranean region shows that convection seems to occur in the same place roughly the same time every year (Send & Marshall 1995). In addition, most of the observations of these convective plumes appear to occur in the Greenland Sea and the Mediterranean region (MEDOC

Group 1970; Schott, Visbeck & Fischer 1993). Upon impacting the stable layer below the mixed layer, deep convective plumes could cause the generation of internal gravity waves that transport momentum from the mixed layer to the deep ocean thereby locally affecting mixing in the deep ocean. Because of the infrequent nature of occurrence of these oceanic plumes, their contribution to the global energy budget associated with internal gravity waves in the ocean is unlikely to be important but the phenomenon is nonetheless interesting to examine.

In the numerical simulations of stratospheric gravity waves using a cloud model and an idealized model of a mechanical oscillator, Fovell *et al.* (1992) observed a fan-like distribution of gravity waves in the stable layer. They explained that the fan-like appearance of waves in their simulations is due to simultaneous forcing by convective plumes at several frequencies. These investigators also pointed out that this aspect of the cloud models is what the single-frequency mechanical oscillator models are not able to mimic.

The study by Pfister *et al.* (1993*a*) traced a transient mesoscale stratospheric gravity wave to a tropical cyclone. The wave generated was studied by using aircraft overflight measurements and satellite imagery, as well as supplementary data of a pilots commentary for the visual description of the overshooting convective turrets. A mechanistic modelling of the gravity wave using a large-scale mechanical oscillator model succeeded, to a large degree, in reproducing the observed wave. They stated that the mechanical oscillator model in their case is the growth and decay of an ensemble of updrafts over a few hours that raises and lowers isentropic surfaces on about a 100 km horizontal scale. An alternative approach using the obstacle effect overpredicted the vertical wavelength of the gravity waves. The poor prediction of the vertical wavelength was attributed to three factors: low mean zonal wind speeds at the measurement height (18.3 km) as compared to the tropopause (16.75 km); the clockwise turning of the mean wind vector with altitude; and the inaccurate placement of the convective forcing relative to the aircraft observations.

Other studies investigating gravity wave generation by deep convection via the mechanical oscillator effect include Lane, Reeder & Clark (2001) and Song, Chun & Lane (2003). They have employed both two and three-dimensional numerical simulations to study waves generated via deep convection and their propagation into the stratosphere. Unlike previous numerical studies that involved two-dimensional quasi-steady long-lived sources, Lane *et al.* (2001) have considered the case of three-dimensional transient sources in their simulations.

One of the first experimental studies designed to investigate the nature of internal gravity waves generated by a thermal (an instantaneous release of a buoyant volume of fluid) was by McLaren *et al.* (1973). The wave field was analysed by studying the trajectories of buoyant marker particles placed in the linearly stratified ambient. It was observed that the waves generated by buoyantly rising fluid at its neutral buoyancy level were transient in nature and had a band of frequencies unlike the waves generated in their experiments using an oscillating solid sphere that had a single frequency. The study did not, however, investigate the energy extracted by the waves from the buoyant element at its stabilizing level.

An experimental study of the energy lost to waves from a thermal was undertaken by Cerasoli (1978). The energy of the internal gravity waves propagating away from the collapse region was estimated by comparing the difference between the initial and final potential energy of the mean state. The energy estimated in this way was found to be 20 %–25 % of the change in potential energy of the whole system.

A recent numerical study has also investigated the generation of gravity waves by thermals via the mechanical oscillator mechanism (Lane 2008). The study concluded

that in a stable ambient fluid, the deceleration and subsequent collapse of a thermal after reaching its neutral buoyancy level are due to a vortical response of the ambient to the overshooting thermal that induces an opposing circulation that inhibits further ascent of the thermal. The response of the vorticity surrounding the thermal was proposed as being responsible for the thermal acting like a damped mechanical oscillator thereby resulting in the generation of the gravity waves.

A theoretical investigation to understand the significance of the energy extracted from a convective element by gravity waves was undertaken by Stull (1976). He modelled penetrative convection as an idealized Gaussian disturbance at the base of a temperature inversion and found that penetrative convection overshooting into a stable temperature inversion from a turbulent mixed layer can excite vertically propagating internal gravity waves in the stable air above the inversion base. He concluded that the amount of energy lost in this way was small if the inversion was strong. However, if the inversion was weak and the convective mixing vigorous, a significant fraction of the energy of the overshooting elements was lost. The inclusion of the inversion layer in the model permitted the propagation of interfacial waves. In the absence of a temperature jump, the theory estimates the maximum amount of energy lost to waves to be about 68 %.

Other studies have examined the internal waves generated due to the motions in a convective layer underlying a stable layer of fluid (Townsend 1964, 1965, 1966; Michaelian, Maxworthy & Redekopp 2002). In particular, Townsend (1964) performed experiments in which fresh water in a tank was cooled to freezing point from below and gently heated from above. The nonlinear relationship between the density of water and temperature resulted in convective motions in the lower layer and the excitation of transient internal gravity waves in the stratified layer above. The rising convective motions were observed to be plume-like rather than spherical thermals and the internal waves were generated due to the penetration of these columnar motions into the stable layer. Michaelian *et al.* (2002) studied the coupling between internal waves and the convective motions in a mixed layer. The convective plumes were initially observed to be vertical and resulted in the generation of high frequency waves, but as the mixed layer grew low frequency waves were generated giving rise to a weak mean flow that in turn modified the plumes from being vertical to being horizontal.

In § 2, we discuss the theory for buoyant plumes and axisymmetric internal gravity waves. We also discuss the theory for the radial intrusion of currents into a linearly stratified environment from a source of constant flow rate. In § 3, we discuss the experimental procedure and provide qualitative results. Quantitative results are presented in § 4. In § 5, we discuss how the results may be extended to geophysical circumstances and summarize our results in § 6.

2. Theory

In the following, we review the theory for forced plumes in a uniform density and linearly stratified ambient fluid. The theory is developed for plumes in which buoyant fluid rises in a denser environment. However, in a Boussinesq fluid, for which the density variations are small compared with the characteristic density, the results are equivalent for a descending dense plume.

2.1. *Equations of motion for a plume*

Forced plumes arise when there is a continuous release of both buoyancy and momentum from a localized source. The flow initially behaves like a jet and gradually

transitions to a pure plume far from the source. Standard reviews on forced plumes may be found in Fischer *et al.* (1979), Chen & Rodi (1980), List (1982) and Lee & Chu (2003). Defining M_0 and F_0 to be the specific momentum and buoyancy fluxes, respectively, at the source, the length scale separating jet-like and plume-like behaviour is given by (Morton 1959; Fischer *et al.* 1979)

$$L_m = M_0^{3/4}/F_0^{1/2}. \tag{2.1}$$

The experiments of Papanicolaou & List (1988) show that the flow is jet-like for $z/L_m < 1$ and plume-like for $z/L_m > 5$, where z is the distance above the virtual origin.

A well-known approach for solving problems of forced plumes is to use the conservation equations of turbulent flow of an incompressible fluid and to employ the Boussinesq and boundary-layer approximations. The resulting equations are typically solved by using the Eulerian integral method (Turner 1973). In this method, a Gaussian or top-hat profile is first assumed for the velocity and concentration profiles of the plume. The equations are then integrated over the plume cross-section and the profiles are substituted into the integral equations. The result is three ordinary differential equations (ODEs) that may be solved numerically or, in special circumstances, analytically. However, an assumption has to be made to close the system of ODEs. This could either be the entrainment hypothesis in which the horizontal flow in the ambient is assumed to be proportional to the axial velocity at that region (Morton, Taylor & Turner 1956) or the spreading hypothesis in which the plume is assumed to widen at a prescribed rate (Abraham 1963; Lee & Chu 2003).

Another approach to modelling plumes is presented by Priestley & Ball (1955). They employed a closure assumption in which the covariance of the velocity fluctuations depended on the square of the mean vertical velocity. A detailed theoretical analyses of the similarities and differences between the models of Priestley & Ball (1955) and Morton *et al.* (1956) have been presented by Morton (1971).

Following the Eulerian approach of Morton (1959), the equations governing the motion of a forced top-hat plume in a linearly stratified environment are given by:

$$\frac{\mathrm{d}Q}{\mathrm{d}z} = 2\alpha\pi^{1/2}\sqrt{M}, \tag{2.2}$$

$$\frac{\mathrm{d}M}{\mathrm{d}z} = \frac{FQ}{M}, \tag{2.3}$$

$$\frac{\mathrm{d}F}{\mathrm{d}z} = -QN^2, \tag{2.4}$$

where M, Q and F are the momentum, mass and buoyancy fluxes, respectively, and N is the buoyancy frequency defined by

$$N^2 = -\frac{g}{\rho_{00}}\frac{\mathrm{d}\overline{\rho}}{\mathrm{d}z}, \tag{2.5}$$

where $\overline{\rho}(z)$ is the background density profile, ρ_{00} is a reference density and g is the gravitational acceleration. These equations assume that the horizontal entrainment velocity is proportional to the axial velocity at each height in which $\alpha = 0.12$ (Kaye 2008) is the proportionality constant.

Given the fluxes of the plume at the source where $z = 0$, (2.2)–(2.4) are used to obtain the fluxes at any distance z above the source. In particular, we first evaluate fluxes at the base of the stratified region after the plume rises a distance H through the uniform-density ambient, where $N = 0$. These interfacial fluxes are then used as the initial conditions to solve (2.2)–(2.4) numerically for rise through a uniformly

stratified fluid. The level of neutral buoyancy z_n is found at the height where the buoyancy flux vanishes and the maximum penetration height z_{max} is estimated as the point where the momentum flux goes to zero.

2.2. *Plume energetics*

The horizontally integrated flux of kinetic energy, F_k, across the horizontal plane of a buoyant plume at height z and the rate of working due to buoyancy forces, W_p, are given respectively by (Turner 1972)

$$F_k = \pi\rho_{00}\int_0^\infty w^3 r\,\mathrm{d}r, \tag{2.6}$$

$$W_p = 2\pi\rho_{00}\int_0^\infty w g' r\,\mathrm{d}r, \tag{2.7}$$

where ρ_{00} is a reference density. Assuming top-hat profiles, (2.6) may be evaluated to get

$$F_k = \frac{1}{2}\rho_{00}\pi\overline{w}^3 b^2, \tag{2.8}$$

where $\overline{w}$ is the average vertical velocity at height z and b is the plume radius. For top-hat profiles, the ratio of the divergence of the kinetic energy flux to the rate of working owing to buoyancy forces is given by (Turner 1972)

$$\frac{\partial F_k/\partial z}{W_p} = \frac{3}{8}. \tag{2.9}$$

Thus, the vertically integrated rate of working of the plume, F_{plume}, from the virtual origin to a height $z = H$ is

$$F_{plume} = \frac{4}{3}\rho_{00}\pi\overline{w}_i^3 b_i^2, \tag{2.10}$$

assuming W_p is zero at the virtual origin. Here $\overline{w}_i$ and b_i are the average vertical velocity and radius of the plume at $z = H$. In the case of a plume in a linearly stratified environment, (2.10) is also used to estimate the rate of working of the plume at its neutral buoyancy level with $\overline{w}_i$ and b_i replaced by the vertical velocity w_n and radius b_n of the plume at the level of neutral buoyancy, z_n.

2.3. *Axisymmetric intrusion speeds*

Upon reaching its neutral buoyancy level, a plume in a stratified fluid first overshoots this level and then falls back to spread radially as an intrusive gravity current. Such radial currents undergo different spreading regimes as they propagate outward (Chen 1980; Didden & Maxworthy 1982; Zatsepin & Shapiro 1982; Ivey & Blake 1985; Lister & Kerr 1989; Lemkert & Imberger 1993; Kotsovinos 2000).

The relationship between the radius of the current, $R(t)$, and time, t, is predicted to be a power law of the form $R(t) \sim t^\kappa$, where κ depends on the particular regime of flow. Four main regimes have been identified in the literature: a regime dominated by the radial momentum flux such that $R(t) \sim t^{1/2}$, a constant velocity regime (Kotsovinos 2000), the inertia-buoyancy regime where $R(t) \sim t^\kappa$ (with $\kappa = 1/2$ by Ivey & Blake 1985, $\kappa = 2/3$ by Chen 1980, $\kappa = 3/4$ by Didden & Maxworthy 1982 and Kotsovinos 2000), and finally the inertia–viscous regime where $R(t) \sim t^{1/2}$. The reasons for the discrepancies in the inertia–buoyancy regime have been addressed by Kotsovinos (2000).

In this study, we measure the initial speeds of the radial currents that spread at the neutral buoyancy level and compare them with theory. We will focus on the first three regimes since we are interested only in the initial speeds. Explicitly, if $V = \mathrm{d}R/\mathrm{d}t$ is the velocity of the intruding fluid, M_R is the radial momentum flux and Q_R is the radial volume flux, then compared to the time scale $t_{MF} = M_R/F_R$, we get

$$V \propto M_R^{1/2}/R, \quad t \ll t_{MF} \tag{2.11}$$

$$V \propto M_R/Q_R, \quad t \approx t_{MF} \tag{2.12}$$

$$V \propto \left(\frac{NQ_R}{R}\right)^{1/2}, \quad t \gg t_{MF} \tag{2.13}$$

where the proportionality constant in (2.13) has been found to be around 0.36 (Kotsovinos 2000). Not all three regimes are necessarily present in a single experiment; the presence of a particular regime largely depends on the competing effects of the radial components of momentum and buoyancy in the flow (Chen 1980; Kotsovinos 2000; Ansong, Kyba & Sutherland 2008).

The radial component of momentum is unknown *a priori*. However, owing to the loss in momentum by moving from a vertical flow to a radial current, we assume that the radial momentum and volume fluxes are proportional to the momentum and volume fluxes of the plume at the neutral buoyancy level (M_n and Q_n, respectively). Thus, from (2.11)–(2.13) and replacing M_R and Q_R by M_n and Q_n, we obtain the expressions that may be used to predict the initial velocity of the axisymmetric currents. The development of the theory above is similar to the approach used by Kotsovinos (2000) and Ansong *et al.* (2008).

2.4. *Representation of axisymmetric internal gravity waves*

The equations governing the motion of small amplitude axisymmetric internal gravity waves in an inviscid and incompressible fluid with no background flow can be reduced to a single equation in terms of the streamfunction $\psi(r, z, t)$:

$$\frac{\partial^2}{\partial t^2}\left[\frac{\partial^2\psi}{\partial z^2} + \frac{\partial}{\partial r}\left(\frac{1}{r}\frac{\partial(r\psi)}{\partial r}\right)\right] + N^2\frac{\partial}{\partial r}\left(\frac{1}{r}\frac{\partial(r\psi)}{\partial r}\right) = 0, \tag{2.14}$$

where the radial and vertical velocities are respectively defined by

$$u = -\frac{\partial\psi}{\partial z}, \quad w = \frac{1}{r}\frac{\partial(r\psi)}{\partial r}, \tag{2.15}$$

and r and z are the radial and vertical coordinates, respectively. Seeking solutions of (2.14) that are periodic in z and t, we find for given vertical wavenumber, k_z, and frequency, ω, that the streamfunction satisfies

$$\psi(r, z, t) = \frac{1}{2}A_\psi J_1(kr)\mathrm{e}^{\mathrm{i}(k_z z - \omega t)} + cc, \tag{2.16}$$

in which cc denotes the complex conjugate, J_1 is the Bessel function of the first kind and order one, and k is defined via the dispersion relation

$$\omega^2 = N^2\frac{k^2}{k_z^2 + k^2}. \tag{2.17}$$

From (2.15) and the implicit definition of the vertical displacement, $w = \partial\xi/\partial t$, the vertical displacement field is represented by

$$\xi = \frac{1}{2}A_\xi J_0(kr)\mathrm{e}^{\mathrm{i}(k_z z - \omega t)} + cc,$$

Field	Structure	Relation to vertical displacement
Vertical displacement	$\xi = \frac{1}{2}A_\xi J_0(kr)\mathrm{e}^{\mathrm{i}(k_z z-\omega t)} + cc$	
Streamfunction	$\psi = \frac{1}{2}A_\psi J_1(kr)\mathrm{e}^{\mathrm{i}(k_z z-\omega t)} + cc$	$A_\psi = -\mathrm{i}\frac{\omega}{k}A_\xi$
Vertical velocity	$w = \frac{1}{2}A_w J_0(kr)\mathrm{e}^{\mathrm{i}(k_z z-\omega t)} + cc$	$A_w = -\mathrm{i}\omega A_\xi$
Radial velocity	$u = \frac{1}{2}A_u J_1(kr)\mathrm{e}^{\mathrm{i}(k_z z-\omega t)} + cc$	$A_u = -\frac{k_z\omega}{k}A_\xi$
Pressure	$p = \frac{1}{2}A_p J_0(kr)\mathrm{e}^{\mathrm{i}(k_z z-\omega t)} + cc$	$A_p = \mathrm{i}\rho_0\frac{\omega^2 k_z}{k^2}A_\xi$
N_t^2	$N_t^2 = \frac{1}{2}A_{N_t^2} J_0(kr)\mathrm{e}^{\mathrm{i}(k_z z-\omega t)} + cc$	$A_{N_t^2} = -k_z\omega N^2 A_\xi$

TABLE 1. Polarization relations and representation of basic state fields for small-amplitude axisymmetric internal gravity waves in the (r, z) plane in stationary, linearly stratified Boussinesq fluid with no background flow. The table also shows the streamfunction and the time derivative of the perturbation squared buoyancy frequency (N_t^2). Each field b is characterized by the phase and magnitude of its complex amplitude, A_b, and the corresponding Bessel functions of the first kind are order zero (J_0) or one (J_1).

where A_ξ is the amplitude of the vertical displacement field and J_0 is the Bessel function of the first kind and order zero. Table 1 shows the representation of other basic state fields in terms of Bessel functions for small-amplitude axisymmetric internal gravity waves.

In practice, we Fourier–Bessel decompose the signal from horizontal time series for $0 \leqslant r \leqslant R$ and $T_1 \leqslant t \leqslant T_2$, and represent

$$\xi(r, z, t) = \sum_n \sum_m \frac{1}{2} A_{\xi nm} J_0(k_n r)\mathrm{e}^{\mathrm{i}(k_z z-\omega_m t)} + cc, \tag{2.18}$$

where $A_{\xi nm}$ is the amplitude of the component of vertical displacement field with frequency $\omega_m = m\omega_0$ with $\omega_0 = 2\pi/(T_2 - T_1)$, radial 'wavenumber' $k_n = \alpha_n/R$ and α_n are the zeros of J_0. Note that k_z is found in terms of k_n and ω_m using (2.17). We only include terms in the sum over m for which $\omega_m \leqslant N$.

Since the waves are assumed axisymmetric, we compute the time-averaged total vertical energy flux, $F_{wave} = \int\int \langle wp \rangle \mathrm{d}A$, using Bessel series and get (see the Appendix)

$$F_{wave} = \frac{1}{4}\pi R^2 \rho_0 N^3 \sum_n \sum_m \cos\Theta_m \sin 2\Theta_m \frac{|A_{\xi nm}|^2 J_1^2(\alpha_n)}{k_n}, \tag{2.19}$$

where p is pressure and Θ_m is the angle of propagation of each wave beam with respect to the vertical satisfying

$$\Theta_m = \cos^{-1}\left(\frac{\omega_m}{N}\right). \tag{2.20}$$

3. Experimental set-up and analyses

3.1. *Experimental set-up*

Experiments were performed in an acrylic tank measuring 39.5 cm long by 39.5 cm wide by 39.5 cm high (see figure 1). These were conducted by injecting dense fluid downward into an initially less dense ambient fluid. The results are dynamically equivalent to injecting light fluid upward from the bottom because the system is Boussinesq. The qualitative results are presented in this section for experiments with and without a uniform-density surface layer. For conceptual convenience and for

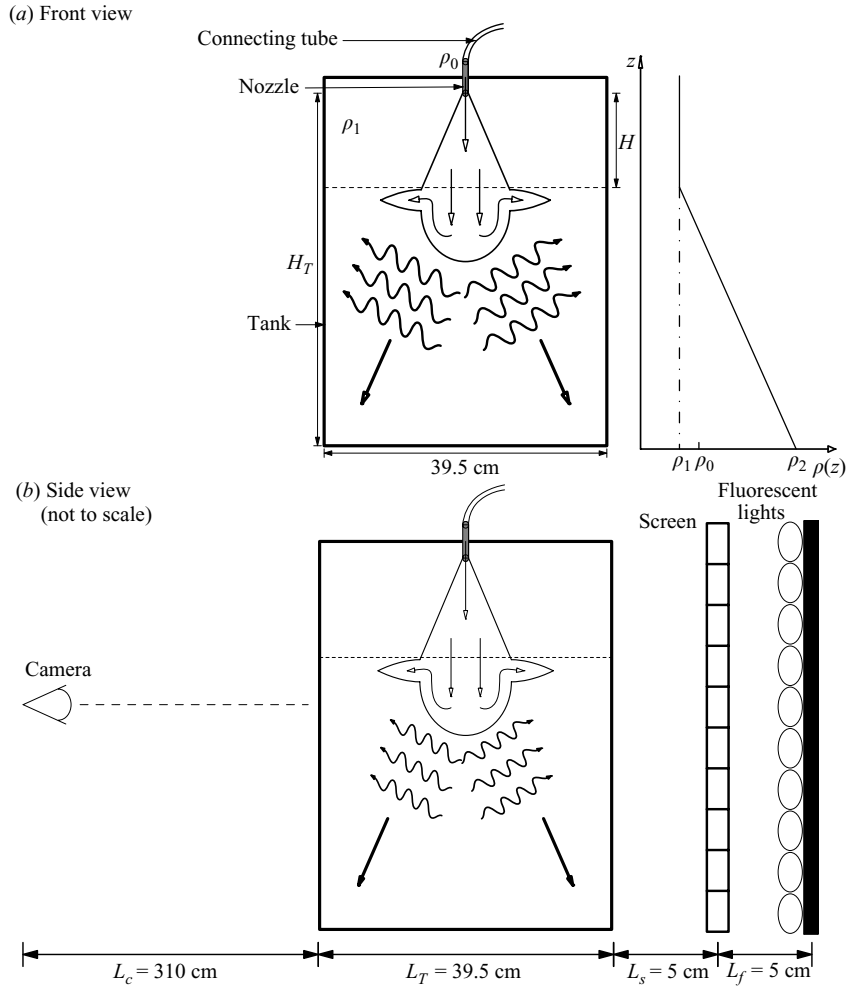

FIGURE 1. (*a*) Front view of the experimental set-up with background density profile and (*b*) side view showing set-up used for synthetic Schlieren.

consistency with the theory presented in § 2, the snapshots from the experiments are flipped upside down so that the plume appears to rise upward.

In all experiments, the total depth of fluid within the tank was $H_T = 38$ cm. In the absence of a uniform-density layer, a linear stratification is set up using the double-bucket technique (Oster 1965). In the presence of a mixed-layer of depth $z = H$, the tank was first filled to a depth $H_T - H$ with fluid whose density increases linearly with depth. Once this height was attained, the flow of fresh water into the salt-water bucket was stopped while the flow from the salt-water bucket into the tank was allowed to continue at the same flow rate. This approach ensured that no density jump was created between the linearly stratified layer and the uniform-density layer. The variations in density were created using sodium chloride solutions and density samples were measured using the Anton Paar DMA 4500 density meter. The density profile in the environment was determined by withdrawing samples from different vertical levels in the tank and by using a vertically traversing conductivity probe (Precision Measurement Engineering). The depth of the mixed layer was varied such

that $H \approx 5,\ 10$ or 15 cm. Figure 1(*a*) shows a schematic of the density variation in the ambient for the case with a mixed layer with $\rho_1 < \rho_2$ where ρ_1 is the density of the mixed layer and ρ_2 is the density at the bottom of the stratified layer.

After the ambient fluid in the tank was established, a reservoir of salt water of density ρ_0 ($\rho_1 < \rho_0 < \rho_2$) was dyed with blue food colouring and then allowed to drain into the tank through a round nozzle of radius 0.2 cm. To ensure that the flow turbulently leaves the nozzle, it was specially designed and fitted with a mesh having openings of extent 0.05 cm. The flow rates for the experiments were recorded by measuring the total volume released during an experiment. Flow rates ranged from 1.7 to 3.3 $\mathrm{cm}^3\,\mathrm{s}^{-1}$.

Experiments were recorded using a single digital camera situated 310 cm from the front of the tank. The camera was situated at a level parallel to the mid-depth of the tank and the entire tank was in its field of view. Fluorescent lighting was placed 10 cm behind the tank to illuminate the set-up (see figure 1*b*). A grid made of horizontal black and white lines was placed between the lighting apparatus and the tank for post-experiment analyses using the synthetic Schlieren method.

Using 'DigImage' software, the maximum penetration depth of the plume and the initial velocity, w_0, were determined by taking vertical time series constructed from vertical slices of movie images at the position of the nozzle. The temporal resolution was as small as 1/30 s and the spatial resolution was about 0.1 cm.

Horizontal time series were used to determine the radial velocity of intrusively spreading gravity currents. They were taken at the vertical position of the neutral buoyancy level.

The generated internal waves were visualized using axisymmetric synthetic Schlieren method (Onu *et al.* 2003; Decamp, Kozack & Sutherland 2008). Apparent distortions of the image of black and white lines were recorded by the camera and the time derivative of their vertical displacement, Δz_t, was estimated by comparing two images taken within a short time interval. Using the Δz_t field, the time derivative of the squared buoyancy frequency, $N_t^2(r, z, t)$, is obtained. The N_t^2 field is useful since it can be used to remove noise by filtering out fast time-scale disturbances. The field is also in phase with the vertical displacement field. The amplitude of the vertical displacement field, $A_{\xi nm}$, for waves with frequency ω_m and radial wavenumber k is calculated from the amplitude of the N_t^2 field, $A_{N_t^2 nm}$, using (see table 1):

$$A_{\xi nm} = -\frac{A_{N_t^2 nm}}{k_z \omega_m N^2}, \tag{3.1}$$

in which k_z is determined using (2.17).

3.2. *Qualitative analyses*

3.2.1. *Experiments with a uniform-density layer*

Figure 2 presents series of spatial snapshots showing the evolution of a plume and the generation of vertically and radially propagating waves. The images on the left of figure 2 are snapshots of the evolving plume and the black and white lines in the images are those of the screen placed behind the tank. The middle column of images are the Δz_t fields revealing the vertical and horizontal structure of distortions resulting from the waves. These depend upon the horizontal x and vertical z coordinates. The Schlieren-processed images on the right also show the structure of the internal waves themselves as they depend upon the radial R and vertical z coordinates.

As is typical of turbulent forced plumes, when the experiment starts, the plume rises due to its positive buoyancy and source momentum, linearly increasing in width as it

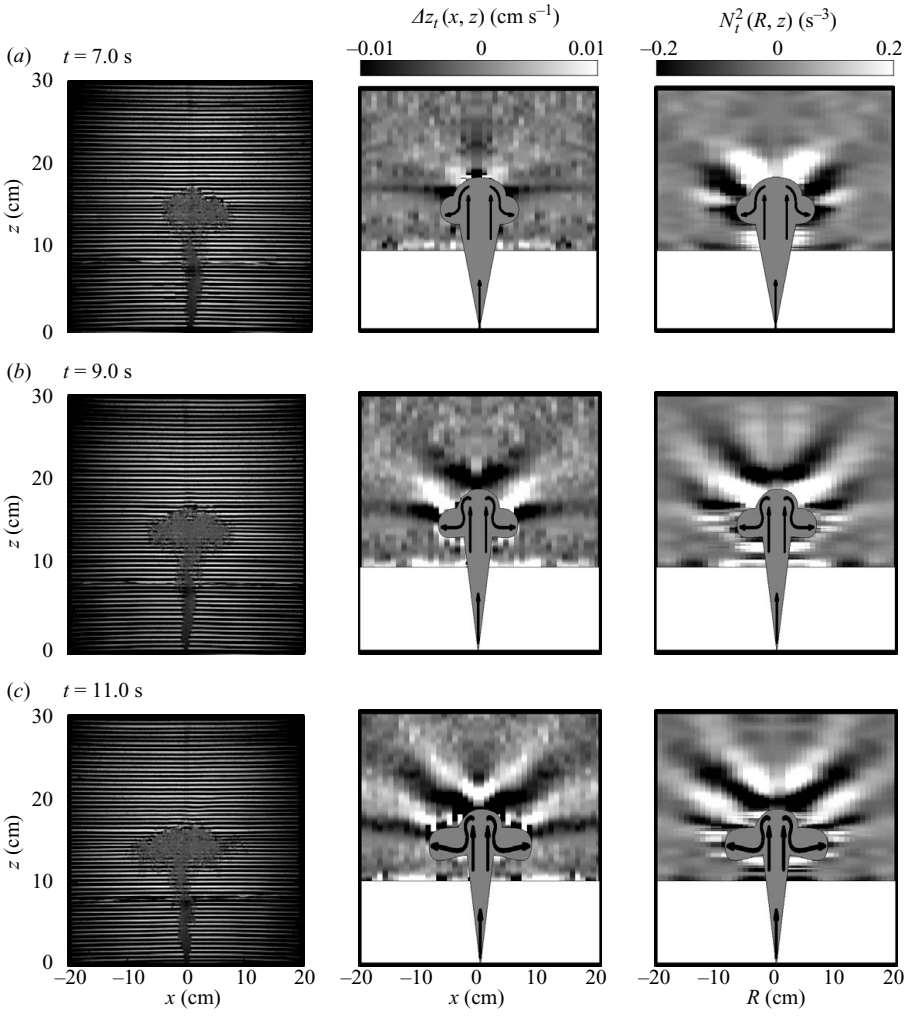

FIGURE 2. Snapshots of plume (flipped upside down and shown on the left), the Δz_t field (middle) and the N_t^2 field of the waves (right) at (*a*) $t \sim 7.0$ s, (*b*) $t \sim 9.0$ s and (*c*) $t \sim 11.0$ s. For the figures in the middle and on the right, the mixed layer region is covered with a white background to highlight the waves and schematics of the plume are superimposed to approximately show its position. The experiment is performed with $\rho_0 = 1.0734\,\mathrm{g\,cm^{-3}}$, $\rho_1 = 1.0363\,\mathrm{g\,cm^{-3}}$, $N = 1.75\,\mathrm{s^{-1}}$, $H \approx 10$ cm, $Q_0 = 3.3\,\mathrm{cm^3 s^{-1}}$.

rises due to entrainment from the ambient. It reaches the interface in a time of about $t \sim 1.5$ s and penetrates beyond the interface to a maximum height of $z \sim 17$ cm in about $t \sim 4.0$ s (not shown). During the initial evolution of the plume as it rises to its maximum height, internal gravity waves are not observed. The waves begin to emanate away from the cap of the plume when it started to fall back upon itself. This is consistent with previous observations of thermals generating internal gravity waves (McLaren *et al.* 1973; Lane 2008). After collapsing upon itself the plume then spreads radially outward as an intrusive gravity current at the neutral buoyancy level.

Figure 3(*a*) shows a horizontal time series taken at the neutral buoyancy level ($z \approx 13$ cm) of the experiment shown in figure 2. The level of neutral buoyancy is usually located by inspecting spatial snapshots of the experiments. The radial

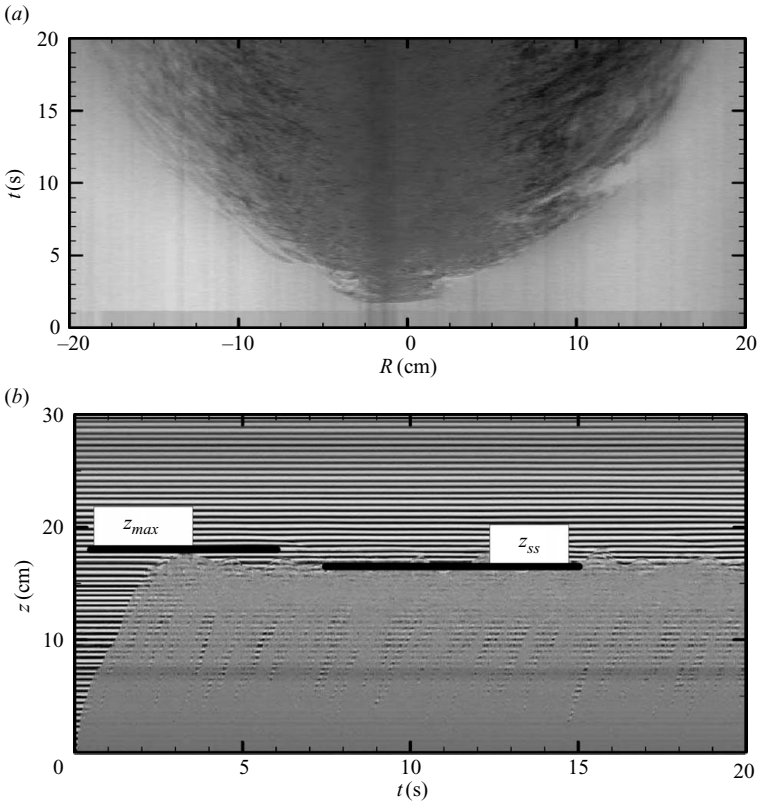

FIGURE 3. (*a*) Horizontal and (*b*) vertical time series of the experiment in figure (2). The horizontal time series is constructed from a slice taken at the neutral buoyancy level, $z \approx 13$ cm. The vertical time series is taken from a vertical slice through the source at $R = 0$ cm.

propagation of the front of the intruding current can be seen. The parabolic nature of the time series shows the change in speed of the front of the current as it spreads towards the tank sidewalls.

Figure 3(*b*) shows a vertical time series taken through the centre of the plume ($R = 0$ cm) illustrating the initial ascension and later vertical oscillatory motion of the plume top with time. This is the same experiment shown in figure 2 in which the plume penetrated to a maximum height $z_{max} \approx 17$ cm. Upon reaching the maximum height, the plume reverses direction due to negative buoyancy and collapses upon itself. The collapsing of the fluid decreases the consequent maximum height of the plume. However, because of the continuous release of fluid from the source, new fluid penetrates the collapsing fluid so as to maintain the plume fluctuating about a quasi-steady-state height z_{ss}. The maximum and steady state heights are indicated in figure 3(*b*).

At time $t \sim 7.0$ s, the rightmost image in figure 2(*a*) shows the waves beginning to emanate from the plume cap. The black and white bands correspond to the troughs and crests respectively of the wave beams. The waves propagate upward and outward towards the tank walls at the same time. A new wave trough appears at $t \sim 9.0$ s (figure 2*b*) above the plume head with approximately the same amplitude as the first trough. At $t \sim 11.0$ s, figure 2(*c*) shows the region above the spreading current completely covered with the wave beams. All this while, the radial current continues to

spread towards the walls of the tank. Nevertheless, the wave beams can still be traced back to the region around the plume cap. This indicates, qualitatively, that the waves are generated by the bulge of fluid at the plume top and not by the spreading currents at the neutral buoyancy level. A quantitative argument supporting this assertion is made by taking the initial spreading speeds of the currents and comparing them with the horizontal phase and group speeds of the waves (see § 4.2).

3.2.2. *Experiments without a uniform-density layer*

Experiments were also conducted for the case in which there was no mixed layer but with a linearly stratified fluid over the whole tank depth. This is the special case in which the uniform-density layer has depth $H = 0$. The evolution of plumes and fountains in linearly stratified environments have previously been studied (Morton *et al.* 1956; Bloomfield & Kerr 1998) but the wave field was not analysed. The wave field is more complex in this case and the linear stratification results in the generation of both upward and downward propagating wave cones by the turbulent plumes.

Figure 4 shows snapshots of a plume as well as the generated internal waves in an experiment with $H = 0$ cm. Similar to the experiment with $H = 10$ cm, waves are not observed until the plume reaches the maximum height and starts to fall upon itself. The plume in this case reaches its maximum height $z_{max} \sim 10$ cm in about 3 s (not shown). At about 6 s (figure 4*a*) we observe the appearance of wave beams around the plume head. Only upward propagating waves are prominent in the wave field at this time even though the appearance of a downward propagating crest and trough can be seen to emanate from around the plume cap. More wave beams are observed in figure 4(*b*) ($t = 7\,s$) with upward propagating waves still prominent. In both figures 4(*b*) and 4(*c*), we observe a cross-pattern of waves resembling the cross-pattern observed in waves generated by oscillating cylinders and spheres (Mowbray & Rarity 1967; Sutherland *et al.* 1999; Sutherland & Linden 2002; Flynn, Onu & Sutherland 2003). The downward propagating waves appear to be generated by the resulting intrusions but nevertheless the phase lines still appear to be radiating from a localized source close to the region below the plume head. In this case the mean depth of the intrusion is about 6 cm from the source. We also note that, despite the different ambient stratifications, the radial scale of the waves is similar both in this case and in the $H > 0$ cases (see figures 2*c* and 4*c*).

3.3. *Bessel–Fourier analyses*

Figure 5 shows the time series and power spectra used to obtain the characteristic frequency and radial wavenumber of the waves.

In figure 5(*c*), the horizontal time series is taken at a vertical position $z = 20$ cm of the experiment shown in figure 2. The plume in this case penetrated to a maximum height $z \approx 17$ cm. Thus, the position $z = 20$ cm is about 3 cm above the maximum penetration height which means that the bulge of fluid from the plume is not captured in the time series; only the radially propagating waves moving up and away from the plume cap are captured.

The horizontal time series shows the radial propagation of the waves with time, and from this we measure the radial and temporal characteristics of the waves. To obtain the characteristic radial wavenumber k_c and frequency ω_c of the waves, we first compute Bessel–Fourier spectra over a specifically chosen window in radial space and time ($0\,\text{cm} \lesssim R \lesssim 20\,\text{cm}$, $1.5 \lesssim t/T_b \lesssim 4.5$) from several horizontal time series taken above the maximum penetration height. Here $T_b = 2\pi/N$ is the buoyancy period. These spectra are then averaged to obtain a characteristic power spectrum of the

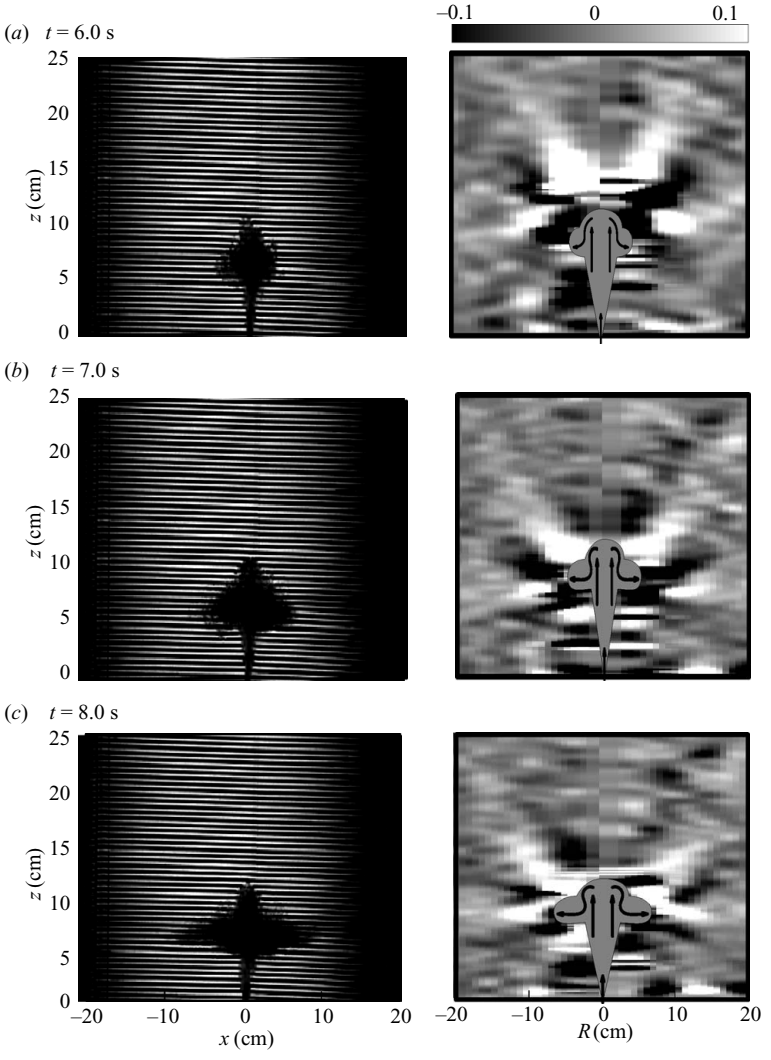

FIGURE 4. Snapshots of plume (flipped upside down and shown on the left) and the N_t^2 field of the waves (shown on the right contours in s^{-3}) at (*a*) $t \sim 6.0\,s$, (*b*) $t \sim 7.0\,s$ and (*c*) $t \sim 8.0\,s$. For the figures on the right, schematics of the plume are superimposed to approximately show its position. (Experiment with $\rho_0 = 1.0720\,g\,cm^{-3}$, $\rho_1 = 1.0310\,g\,cm^{-3}$, $N = 1.43\,s^{-1}$, $Q_0 = 3.2\,cm^3 s^{-1}$, $H = 0\,cm$).

waves. For example, the average power spectrum shown in figure 5(*b*) was obtained by Fourier-transforming in time and Bessel-transforming in the radial direction over several rectangular windows such as the one shown in figure 5(*c*) extracted from images of the experiment shown in figure 2. In this case, the horizontal slices are taken in the range $20\,cm \leqslant z \leqslant 25\,cm$ and the time interval is $7\,s \leqslant t \leqslant 25\,s$. Choosing a window avoids the inclusion of the reflected wave beams from the sidewalls of the tank. From the power spectrum, we observe that the waves are quasi-monochromatic. Averaging over all radial wavenumbers gives the frequency spectrum in figure 5(*a*). This shows a peak frequency $\omega \approx 1.1\,s^{-1}$. However, there is non-negligible power in neighbouring frequency components and so a characteristic frequency of the waves is

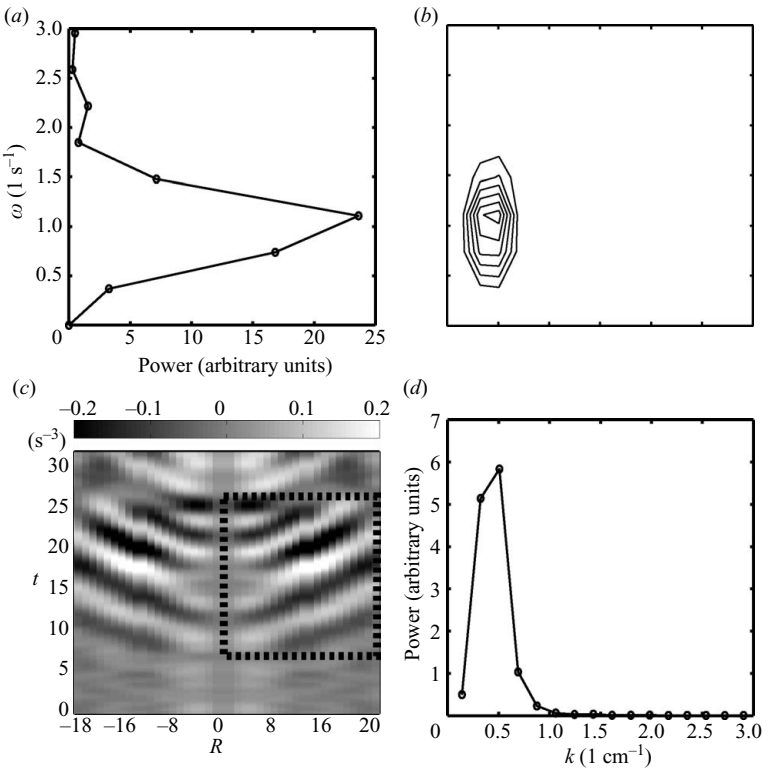

FIGURE 5. (*a*) Frequency spectrum obtained by averaging over all radial wavenumbers in (*b*), where (*b*) shows the average power spectrum from different horizontal time series taken over the rectangular window shown in (*c*). (*c*) is a horizontal time series taken at $z = 20\,\text{cm}$ of the experiment in figure 2. The horizontal slices are taken in the range $20\,\text{cm} \leqslant z \leqslant 25\,\text{cm}$ and $7.0\,\text{s} \leqslant t \leqslant 25\,\text{s}$ (rectangle with dashed lines). (*d*) Radial spectrum obtained by averaging over all frequencies in (*b*). Experimental parameters are the same as in figure 2.

found by calculating a power-weighted average:

$$\omega_c = \frac{\sum_m \omega_m |A_{\xi m}|^2}{\sum_m |A_{\xi m}|^2}.$$

Computed in this way, the characteristic frequency of the waves in this case is found to be $\omega_c = 1.0\,\text{s}^{-1}$ and the value of $N = 1.75\,\text{s}^{-1}$.

Averaging over all frequencies gives the radial spectrum shown in figure 5(*d*) with a peak radial wavenumber $k \approx 0.5\,\text{cm}^{-1}$. The figure also shows that most of the radial power lies in the second and third modes. A characteristic radial wavenumber is obtained by calculating a power-weighted average to get $k_c = 0.4\,\text{cm}^{-1}$.

4. Quantitative analyses

In this section, we give a quantitative analyses of the results and compare them with theory. In the experiments without a uniform layer of fluid ($H = 0$), only the upward propagating waves have been included in the analyses.

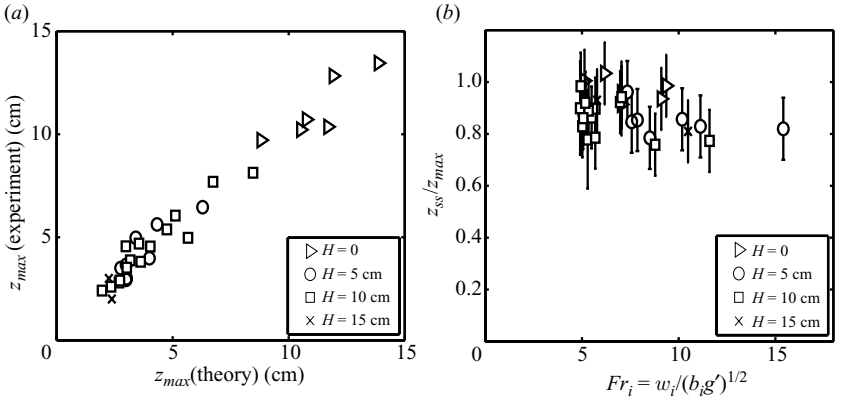

FIGURE 6. (*a*) The maximum penetration height above the interface and (*b*) the ratio of the steady-state height to the maximum height.

4.1. *Maximum penetration height*

Figure 6(*a*) shows the experimentally measured values of the maximum penetration height above the interface compared with the theoretical prediction of Morton (1959). The maximum plume height z_{max} is computed by numerically solving (2.2)–(2.4) using values of M, F and Q evaluated at the interface. There is good agreement in the data with a correlation of about 90 %. Figure 6(*b*) is a plot of the ratio z_{ss}/z_{max} against the interfacial Froude number, Fr_i. The average value of this ratio was found to be 0.90 ± 0.1. Morton *et al.* (1956) did not measure the quasi-steady-state height in their experiments of a plume in a linearly stratified ambient; however we find that this ratio compares well with the case of a fountain in a linearly stratified environment measured by Bloomfield & Kerr (1998) to be 0.93. This value is slightly greater than the ratio obtained for a fountain in a two-layer density-stratified ambient in which the ratio is about 0.88 (Ansong *et al.* 2008). Although within errors, the ratio may also be due to the greater interaction of the descending annular plume with the main upflow in the case of a fountain in a two-layer ambient as compared with a plume in a stratified environment in which the distance of interaction is between the maximum height and the neutral buoyancy level.

4.2. *Radial intrusion speeds*

The main goal of measuring the initial speeds of the axisymmetric currents is to show that the measured waves are those generated by the vertical fluctuations of the plume and not the radially spreading currents.

Figure 7 shows the experimentally measured values of the level of neutral buoyancy, z_n (see figure 11), compared with the theoretical prediction of (2.2)–(2.4) using values of M, F and Q evaluated at the interface. Theoretically, the level of neutral buoyancy is taken as the height at which the buoyancy flux first vanishes. In the experiments, the neutral level is visually determined from spatial snapshots after the intrusion is established. There is good agreement in the data with a correlation of about 95 %. Only experiments with the neutral buoyancy level greater than 0.5 cm from the interface are plotted. This is because the neutral buoyancy level is usually indistinguishable from the interface for $z_n < 0.5$ cm and besides the error involved in measuring the position of the interface is about 0.3 cm.

The relationship between theory and experiment is surprisingly good considering the fact that the theory, as applied here, assumes that there is no mixing of ambient

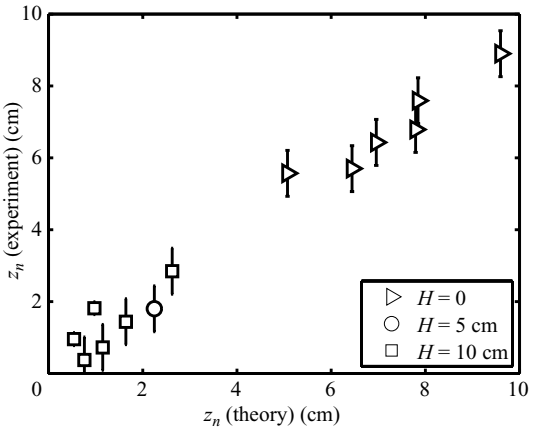

FIGURE 7. Intrusion height, z_n, of the radial currents for experiments with $z_n > 0.5$ cm.

fluid between the neutral level and the maximum height. This is probably because the axial velocity of the plume continues to decrease from the neutral buoyancy level until it finally comes to rest at the maximum height. Therefore, the assumption that entrainment is proportional to the axial velocity implies that there is less entrainment in this part of the plume motion (Morton *et al.* 1956). A similar assumption was used by Abraham (1963) to model the topmost part of turbulent fountains where it was assumed that there is detrainment rather than entrainment of ambient fluid.

The initial speeds of the axisymmetric currents were measured by taking the slope near $R \approx R_n$ of horizontal time series as shown, for example, in figure 8(*b*). R_n is the width of the plume at the neutral buoyancy level that is determined from horizontal time series such as in figure 8(*a*). Both the left- and right-moving current speeds are measured and the average used to estimate the initial speeds.

Figure 8(*c*) shows a typical log-log plot of distance against time taken from figure 8(*b*). This is used to determine the appropriate initial scaling relationship between distance and time for the intrusions. All the experiments were found to spread initially as $R \sim t^{\kappa}$, with $\kappa = 1.0 \pm 0.1$. Figure 8(*d*) shows the initial spreading speeds of the intrusion compared with (2.12) with the initial radial momentum and volume fluxes replaced by those of the plume at the neutral buoyancy level. The plot shows a relationship of the form

$$V = (0.12 \pm 0.02)\left(\frac{M_n}{Q_n}\right). \tag{4.1}$$

Figures 9(*a*) and 9(*b*) show the initial speed of the intrusion against the radial phase speeds and group velocities of the waves respectively. Both plots show a poor relationship between the respective parameters. This provides further support to the assertion that the waves are generated by a localized source around the plume cap and not by the intrusion currents. Although the intrusions may also generate waves, these are not the dominant waves measured in the experiments above the maximum penetration height. Moreover, the waves were observed to be generated long before the intrusion is well established.

4.3. *Radial wavenumber*

Since the most obvious horizontal scale of the generating source is the width of the plume at the density interface, one might expect that the radial scale of the waves

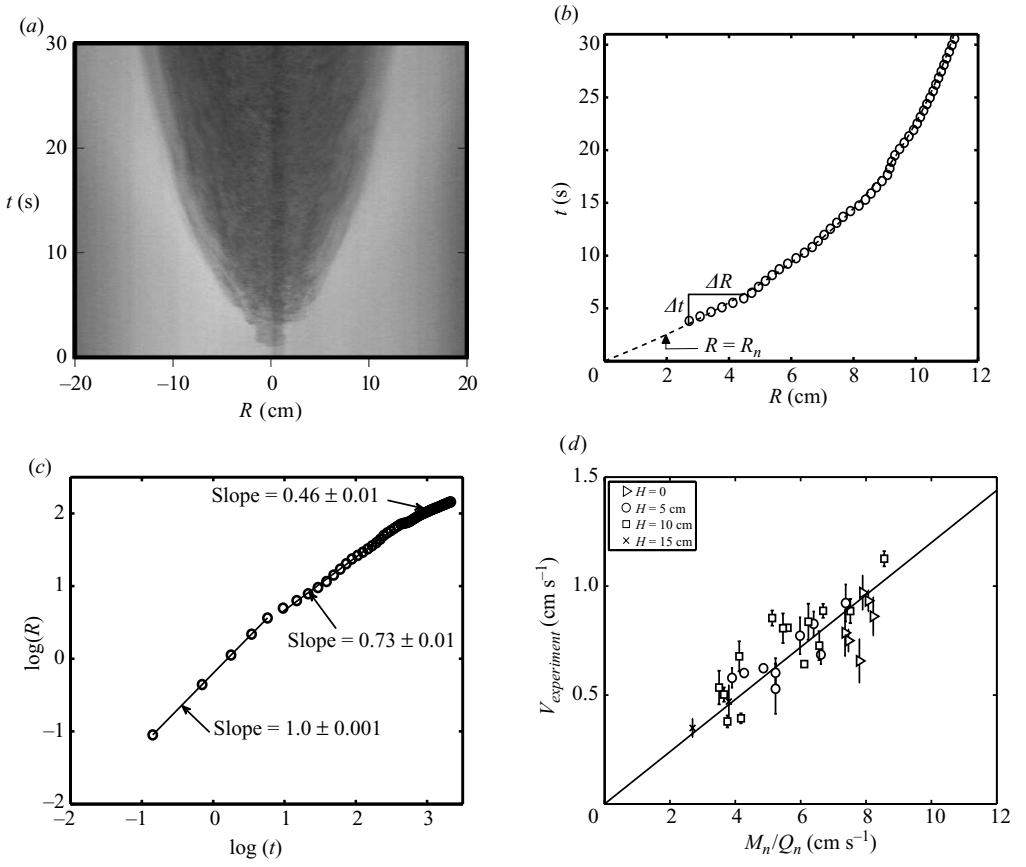

FIGURE 8. (*a*) Horizontal time series for an experiment with $N = 1.62\,\mathrm{s}^{-1}$, $H = 5\,\mathrm{cm}$, $\rho_0 = 1.0544\,\mathrm{g\,cm}^{-3}$, $\rho_1 = 1.0511\,\mathrm{g\,cm}^{-3}$. The time series was constructed from a slice taken at the neutral buoyancy level ($z \approx 5.2\,\mathrm{cm}$). (*b*) Typical approach of calculating the initial spreading speeds with $\Delta R \approx R_n$ (the width of the plume at the neutral buoyancy level) and Δt is the time taken to travel the distance ΔR. ○, experimental data; …, fitted line. (*c*) The log-log plot of the horizontal time series showing the different spreading regimes. (*d*) Plot of the initial spreading speeds for all experiments.

is set by this parameter. To investigate this, experiments with varying mixed layer depths were conducted.

Figure 10(*a*) shows the inverse of the characteristic radial wavenumber against the radius of the plume at the interface, b_i, for all the experiments. We observe that $k_c^{-1} \approx 2.0\,\mathrm{cm}$ is almost constant for experiments with different mixed layer depths ($H \approx 0$, 5, 10, 15 cm) and therefore for different plume radii at the interface. The source radius is used in the case $H = 0$ and has also been plotted in figure 10(*a*). The lack of correlation in the experiments show that the radial scale of the waves is not set by the width of the plume at the density interface. This is unlikely to be caused by the effects of the tank size since the radial scale of the waves is set before the waves reach the sidewalls of the tank (e.g. see figure 2).

Because we start observing the waves when the plume begins to fall upon itself, we hypothesize the scale of the waves is set by the radius of the plume cap just after the plume reached the maximum height. For each experiment, three measurements of the plume cap radius were taken within one second of each other after the plume reached

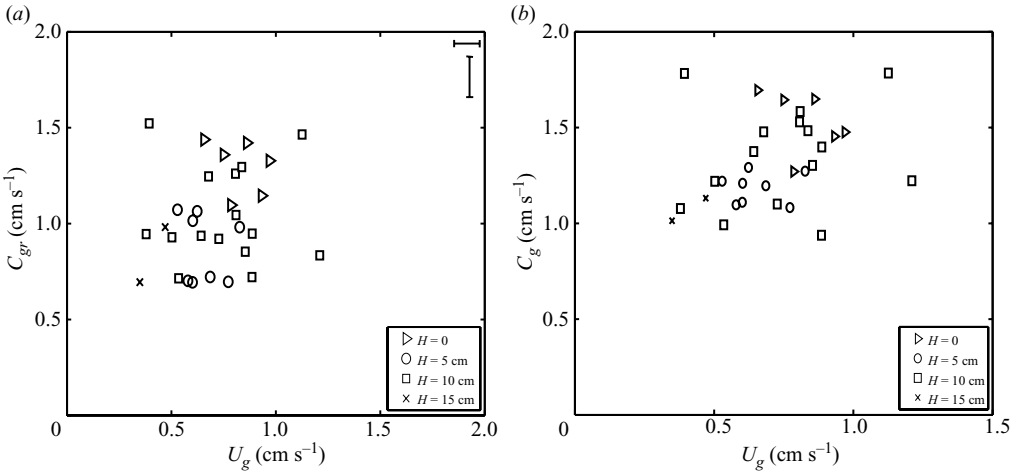

FIGURE 9. Radial intrusion speed, U_g, vs. (*a*) the radial phase speed, c_{gr}, and (*b*) the group speed, c_g, of the waves. Characteristic error bars are shown at the top right corner in (*a*).

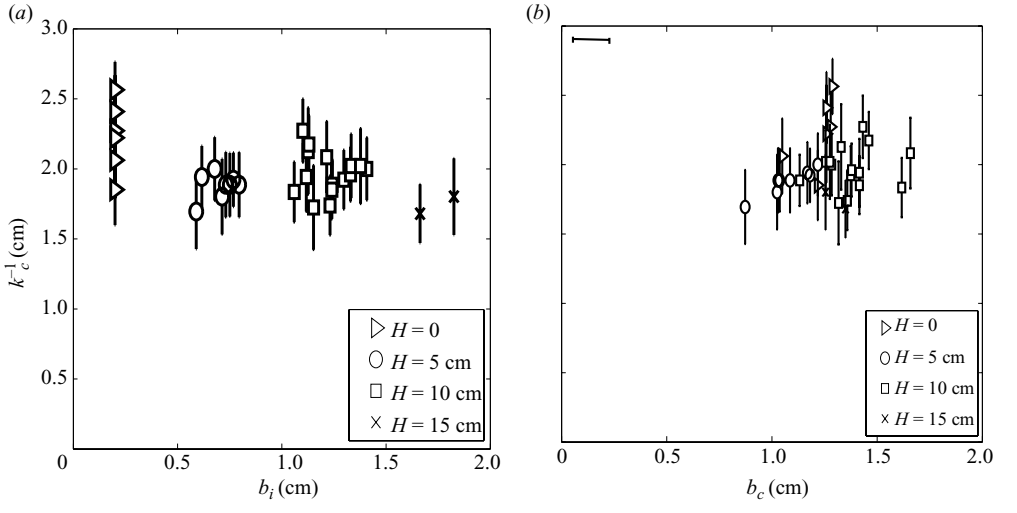

FIGURE 10. The inverse characteristic radial wavenumber as a function of (*a*) the radius of plume at the interface for the uniform-density layer case (the source radius is used on the x-axis in the case $H = 0$ cm) and (*b*) the mean radius of the plume cap. Characteristic error bar for b_c is shown at the top left corner.

the maximum height. The measurements were taken at a vertical level midway between the maximum height and the neutral buoyancy level (see figure 11). The average of these radii was used as the radius of the cap, b_c. Figure 10(*b*) shows the inverse of the characteristic radial wavenumber against the mean radius of the cap. We find that the radius of the cap generally lies between values of 1.0 cm and 1.7 cm comparable to k_c^{-1} for different values of H. It, therefore, appears that the characteristic radial wavenumber is set by the mean radius of the plume cap after it collapses upon itself and not upon the radius of the incident plume at the interface height. What determines the horizontal extent of the plume cap, as it depends upon Q, M and F, is not yet well established in theory. Indeed, numerical and theoretical attempts to

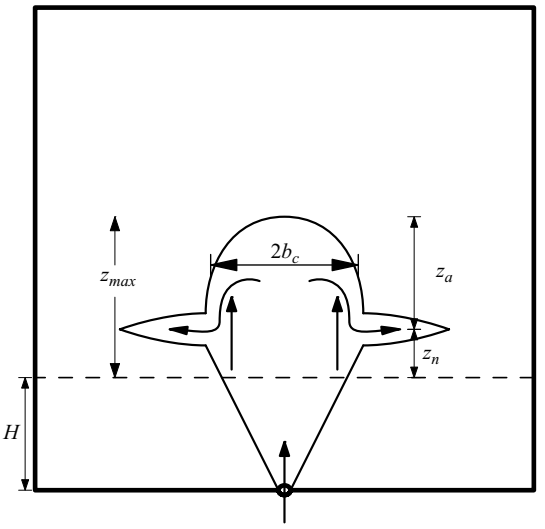

FIGURE 11. Schematic showing the position where the radius of the plume cap, b_c, the maximum penetration height, z_{max} and neutral buoyancy level, z_n, are measured. z_a is the distance above the neutral buoyancy level.

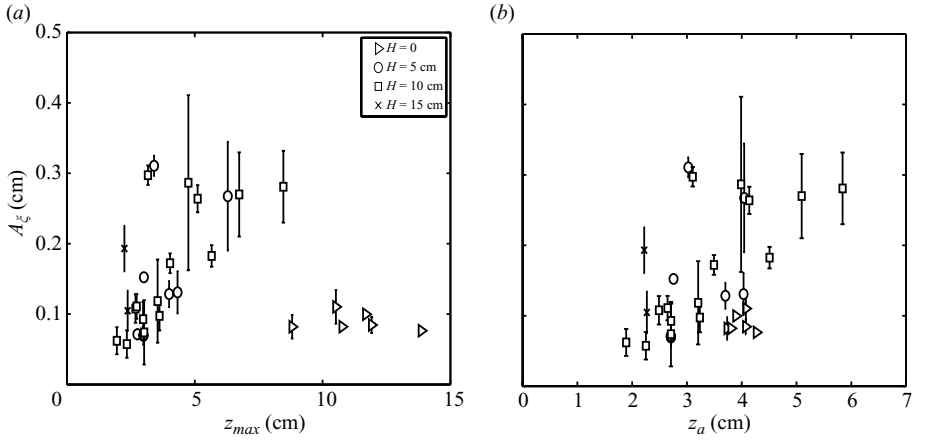

FIGURE 12. Vertical displacement amplitude of waves, A_ξ, vs. (*a*) the maximum penetration height and (*b*) penetration above the neutral buoyancy level.

model the dynamics of the plume cap rely on heuristic methods (McDougall 1981; Bloomfield & Kerr 2000).

4.4. *Vertical displacement amplitude*

One might expect that the amplitude of the waves would depend upon the maximum penetration height of the plume into the stratified layer. This is because the greater the penetration of the plume into the linearly stratified layer, the greater is the displacement of the isopycnals above the plume cap.

Figure 12(*a*) shows the theoretical maximum penetration of the plume against the maximum vertical displacement amplitude, A_ξ, that is measured in the wave field. The amplitudes are obtained from horizontal time series taken about 3 cm above the maximum penetration height. This enables us to measure the near-maximum

amplitudes of the waves without corruption of the signal by the plume itself that would occur by taking measurements too close to the plume. For the $H > 0$ cases, the trend in the plot suggests a strong linear dependence of the amplitude upon the maximum penetration depth within the limits of the experimental parameters. Even though the $H = 0$ cases penetrated further into the stratified ambient, their amplitudes are not as large. They have an almost constant amplitude around 0.1 cm. This means that the maximum penetration height does not properly characterize the amplitude of the waves. In figure 12(*b*), we have plotted the vertical displacement amplitude against the penetration of the plume beyond its neutral buoyancy level, z_a (see figure 11). The trend indeed shows a linear relationship for all cases even though there is less variation in z_a for the $H = 0$ cases. The linear trend in figure 12(*a*) for the $H > 0$ cases may also be due to the fact that most of those experiments had their neutral buoyancy levels close to the interface height so that z_{max} is approximately equal to z_a as explained in § 4.2.

Caution needs to be taken in interpreting this result since the amplitudes of the waves are not expected to increase to infinity with increasing maximum penetration. Experiments with larger penetration depths could not be examined because we needed to ensure that there was sufficient vertical and horizontal space for analysing the waves in the limited domain of the tank. The time it takes for waves to reach the walls of the tank after generation can be estimated based upon their group velocity (see figure 9*b*) and characteristic frequency (see figure 14). Assuming that the waves emanated from the centre of the plume at the maximum height in a tank of radius $\sim$ 20 cm, we estimated that it takes 13–36 s for the waves to reach the tank walls depending on the experiment.

It is also important to recognize the different dynamics involved in the $H > 0$ and $H = 0$ cases. In the $H > 0$ case, the plume is largely controlled by buoyancy forces as it enters the stratified layer since its initial momentum is mostly used up by the time the plume impinges the interface. So its dynamics within the stratified layer is roughly the case of a pure plume in a linearly stratified environment. On the other hand, in the $H = 0$ case, the plume enters the stratified layer as a forced plume, being controlled initially by the momentum at the source and later by buoyancy forces. Thus, even though the plume in the $H = 0$ case travelled farther in the stratified layer, it does not necessarily have a higher overshooting distance. In general, the overshooting distance largely depends on the excess momentum at the neutral buoyancy level which, in turn, depends upon the strength of the stratification and the fluxes of buoyancy and momentum at the source.

4.5. *Wave frequency versus forcing frequency*

When the plume reaches the initial maximum height, it falls upon itself because of its negative buoyancy and, subsequently, it oscillates about a quasi-steady-state depth. Though these oscillations appear random, to our knowledge, they have not been analysed before to determine their spectral characteristics. Turner (1966) observed that the quasi-steady fluctuations of salt water fountains in one-layer fresh water environments were small and random. On the contrary, the fluctuations from 'evaporating' plumes (composed of various mixtures of alcohol and ethylene glycol) were observed to be more dramatic in that they were more regular and with larger amplitudes. The amplitudes decreased with time but eventually achieved the same mean height as the salt water fountains (see figure 3 of Turner 1966).

In figure 13(*a*), we plot the fluctuations from an experiment with buoyancy frequency $N = 1.17\,\mathrm{s}^{-1}$. These were determined by taking a vertical time series through

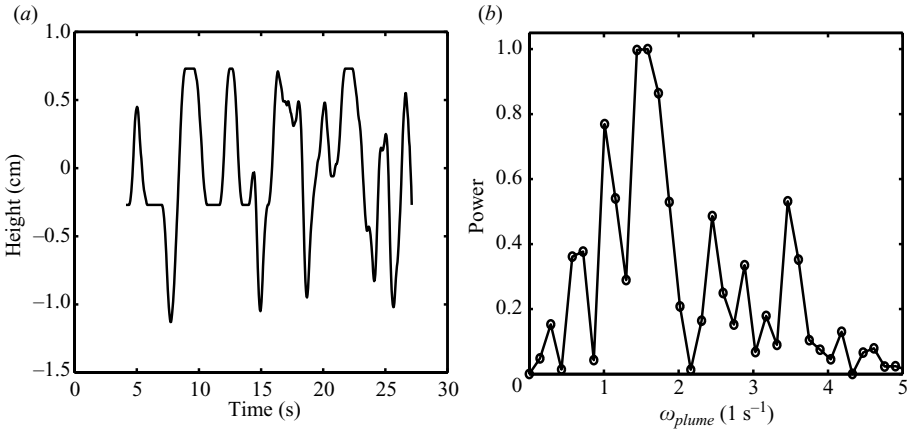

FIGURE 13. (*a*) Vertical time series through the centre of a plume with parameters: $\rho_0 = 1.0400\,\mathrm{g\,cm^{-3}}$, $\rho_1 = 1.0230\,\mathrm{g\,cm^{-3}}$, $N = 1.17\,\mathrm{s^{-1}}$, $Q_0 = 2.15\,\mathrm{cm^3 s^{-1}}$, $H \approx 5\,\mathrm{cm}$. The vertical fluctuations are subtracted from their mean value to get the vertical axis. (*b*) The frequency spectrum of the signal in (*a*) with the power normalized by the maximum power.

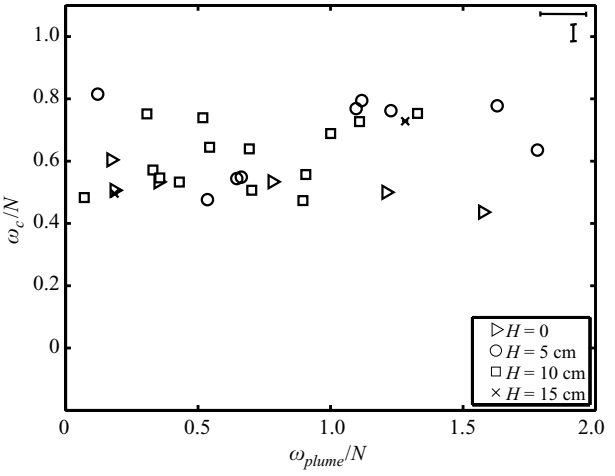

FIGURE 14. Peak forcing frequency of the plume, ω_{plume}, vs. the frequency of the waves both normalized by the buoyancy frequency. Characteristic error bars are shown at the top right corner.

the centre of the plume and the extent of the vertical fluctuations were subtracted from their mean values. The figure shows a quasi-regular pattern of oscillations. A Fourier decomposition of the signal gives the frequency spectrum shown in figure 13(*b*). The spectrum exhibits a wide range of frequencies with a peak frequency around $1.6\,\mathrm{s^{-1}}$, greater than the buoyancy frequency of the stratified layer and greater than the characteristic frequency of the generated waves ($\omega_c \approx 1.0\,\mathrm{s^{-1}}$ in this case). Figure 14 shows a plot of the peak frequency of the plume, ω_{plume}, versus the frequency of the waves illustrating that there is no direct linear relationship between the two parameters. Thus, unlike internal gravity waves generated by solid objects (such as spheres and cylinders) undergoing small amplitude oscillations (see Mowbray & Rarity 1967; Sutherland *et al.* 1999; Sutherland & Linden 2002; Flynn *et al.* 2003), waves generated by turbulent forced plumes have peak frequencies that do not directly relate to the observed fluctuations of the plume cap itself.

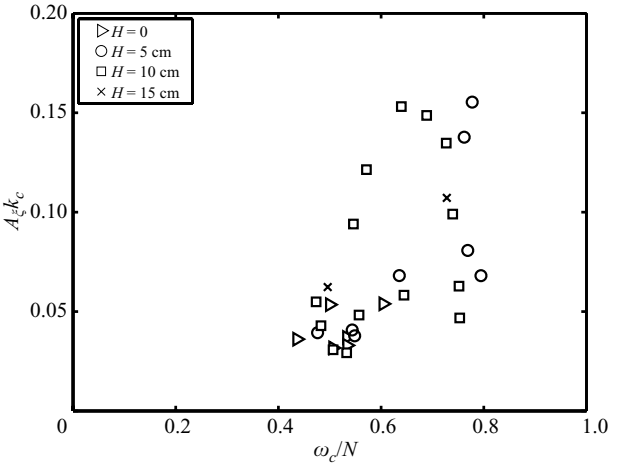

FIGURE 15. Relative frequency of the waves vs. the normalized amplitude.

Both figures 14 and 15 further show that the characteristic frequency of the waves generated by the turbulent plumes lie in a narrow frequency range ($0.45 \leqslant \omega_c/N \leqslant 0.85$). This is consistent with the findings of Dohan & Sutherland (2003), in which the waves generated by turbulence were found to lie in a narrow frequency range ($0.5 \leqslant \omega/N \leqslant 0.75$). They hypothesized that turbulent eddies generating internal gravity waves interact resonantly with the waves in a manner that most strongly excites those waves that vertically transport the most horizontal momentum (Sutherland, Flynn & Dohan 2004; Dohan & Sutherland 2005). The vertical flux of horizontal momentum away from the generation region is proportional to $\rho_0 N^2 A_\xi^2 \sin(2\Theta)$; so that for a fixed displacement amplitude the maximum value of the momentum flux occurs at $\Theta = 45°$. The dominant waves in our experiments propagate with Θ in the range 32°–63° with a mean value of around 45°. Such waves exert the most drag on the source and so are most efficient at modifying the structure of eddies that excite them.

Note that some numerical cloud models also reveal that the dominant frequency of gravity waves generated via the mechanical oscillator mechanism lie in a narrow range. For example, in the two-dimensional cloud-resolving numerical model of Song *et al.* (2003), a well-defined peak period of 18.1 min (corresponding to $\omega_c \approx 0.0058\,\mathrm{s}^{-1}$) in an environment with $N = 10^{-2}\,\mathrm{s}^{-1}$ was observed. This implies that $\omega_c/N = 0.58$ and lies in the relative frequency range observed in our experiments.

4.6. *Energy extraction by waves*

The rate of working owing to buoyancy forces of the plume at the neutral buoyancy level was calculated from (2.10) by replacing the radius and velocity at the interface with those at the neutral level. The average wave energy flux was calculated using (2.19). This was derived by assuming that the waves generated were symmetric about the centre of the tank. To verify this, energy fluxes from the left and right sides of the tank were independently determined and the average energy flux was calculated. Separately, the N_t^2 fields from the left and right sides of the tank were first averaged and the mean energy flux calculated. The difference in the energy fluxes between the two approaches approximately gives the error involved in the assumption of axisymmetry. The asymmetry in the wave field is usually caused by the tilting to one side of the plume cap from the centreline as the plume falls upon itself. This

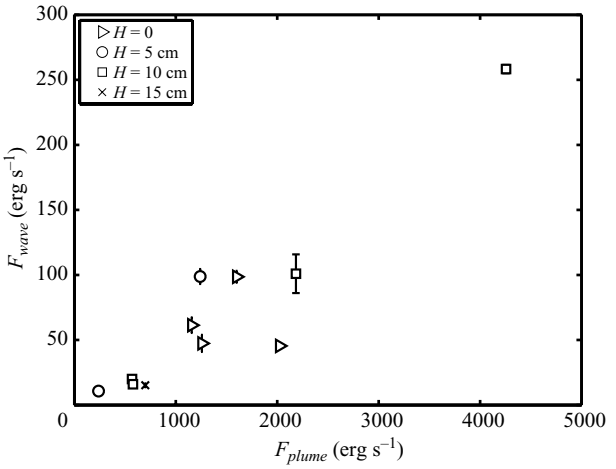

FIGURE 16. The energy flux of the plume at its neutral buoyancy level vs. the energy flux of the waves.

behaviour is difficult to control even if the initial injection of plume fluid is kept vertical.

Using the above criteria, if the difference between the two calculations is greater than 20 %, the experiment is considered asymmetric and is not included in the analyses of the energy fluxes. We find that about 30 % of the experiments had differences to within 20 %.

Figure 16 shows the estimated energy flux of the plume at its neutral buoyancy level against the mean energy flux of the waves (calculated by taking the average of the energy fluxes from the left and right sides of the tank). The average energy flux of the waves for each side of the tank is estimated by vertically averaging energy fluxes over a 4 cm interval ($z_{max} + 3\,\mathrm{cm} \lesssim z \lesssim z_{max} + 7\,\mathrm{cm}$) in order to capture any vertical fluctuations in the energy flux due to the transient and turbulent nature of the source. This vertical range was also chosen to avoid reflected waves from the sidewalls and bottom of the tank. There appears to be a linear relationship between the two parameters. We find that 0.1 %–8 % of the energy flux of the plume at its neutral level is extracted by the waves. The average energy extracted is about 4 % for the experiments considered. Although so small, this should not influence the large-scale plume dynamics. This is plausibly large enough to influence the eddy dynamics at the boundary between the plume cap and ambient.

5. Application to convective storms

The percentage of energy extracted by waves from plumes may be substantial when compared with the enormous amount of energy released by thunderstorms.

The study by Pierce & Coroniti (1966) first proposed that gravity waves may be generated by severe thunderstorms via oscillations of the updrafts within the storm. They stated that the updraught extends throughout most of the cell and are generally of the order of 3 m s^{-1} but may locally exceed 30 m s^{-1}. Using observational data they were able to estimate the energy per unit volume to be on the order of 1.0 erg cm^{-3}. Assuming that the oscillations extended over an area roughly 10 $\times$ 10 km and over a height interval of 3 km, they estimated the total energy of the oscillation to be 3×10^{10} J.

Curry & Murty (1974) showed through field observations that internal gravity waves are generated by thunderstorms through the transfer of kinetic energy from a rising column of air within the storm cell to a stable region aloft. In a case study, the amplitude spectra showed that the wave consisted essentially of a single component having a period of ~ 16 min and a buoyancy period of 25.0 min ($N \approx 0.004\,\mathrm{s}^{-1}$) that is larger than the observed period of the waves.

They proposed a simple model for the generation of gravity waves by thunderstorms based on energy considerations. The top of the developing thunderstorm cell was assumed to be a hemispherical cap of radius $\tilde{R}$ and rising with velocity U. It was assumed to interact with waves at its position of stability where it oscillates at a characteristic frequency. The kinetic energy (KE) carried into the source was then calculated as

$$\mathrm{KE} = \frac{\pi}{3}\tilde{R}^3 U^2 \rho_a, \tag{5.1}$$

where ρ_a is the density of the air. An order of magnitude calculation was carried out to find the value $\mathrm{KE} \approx 5 \times 10^9$ J, where ρ_a was taken as $0.5\,\mathrm{kg\,m^{-3}}$, the value of $\tilde{R}$ was 500 m and $U = 10\,\mathrm{m\,s^{-1}}$ were used. The rough estimate of the kinetic energy from their model was found to agree well with an estimate from their case study where the kinetic energy was found to be 6×10^9 J.

We recast (5.1) in terms of the energy flux at the source to get

$$F_{storm} = \frac{1}{2}\pi\tilde{R}^2 U^3 \rho_a. \tag{5.2}$$

Using the values of Curry & Murty (1974) results in $F_{storm} \approx 1.3 \times 10^{15}\,\mathrm{ergs\,s^{-1}}$.

Other observational studies of gravity waves generated by thunderstorms include Balachandran (1980), Larsen, Swartz & Woodman (1982), Lu, VanZandt & Clark (1984), Gedzelman (1983), Pfister, Scott & Loewenstein (1993*b*), Pfister *et al.* (1993*a*), Alexander & Pfister (1995), Grachev *et al.* (1995), Karoly, Roff & Reeder (1996) and Dewan & Coauthors (1998). In particular, Larsen *et al.* (1982) observed that waves are generated only when the vertical extent of the developing clouds approaches the level of the tropopause. However, like other observational studies of thunderstorm-generated waves, the details of the horizontal scale of the storm as well as the speeds of the updrafts could not be obtained. One of the difficulties is the fact that the storms themselves are not stationary but vary in both space and time. Another problem is that the observational techniques are unable to provide this information on the storms (Lu, VanZandt & Clark 1984; Fritts & Alexander 2003). Aircraft measurements and satellite imagery usually provide information on the horizontal scale of the storms and limited information on updraft speeds (Pfister *et al.* 1993*b*,*a*; Dewan & Coauthors 1998). Nevertheless, the information provided by aircraft measurements about the characteristics of the generated waves is not enough to help make a concrete quantitative link between the energy flux of the waves and the storms. Some observational studies show that the horizontal scale of the waves are comparable with the horizontal scale of the storms (Pfister *et al.* 1993*a*; Tsuda *et al.* 1994). The periods of the waves have been reported by some observations to be close to the local buoyancy period (Pierce & Coroniti 1966; Curry & Murty 1974; Larsen *et al.* 1982) while others observe thunderstorm-generated waves to have periods longer than the buoyancy period (Lu *et al.* 1984). The results of the laboratory experiments presented here show that depending upon the strength of convection, the mechanical oscillator

mechanism could contribute on average 4 % of the energy flux of the thunderstorm to the waves.

The waves generated by thunderstorms have been reported to have horizontal wavelengths in the range of 5–110 km, vertical scales in the range of 2–7 km, periods ranging between 5 min and 3 h and with phase speeds in the range of 12–30 m s^{-1} (Larsen *et al.* 1982; Lu *et al.* 1984; Pfister *et al.* 1993*b*,*a*; Karoly *et al.* 1996; Vincent & Alexander 2000). Thus, in general, convective sources generate waves with a broader spectrum than topographically generated waves (Fritts & Alexander 2003). The study by Fritts & Nastrom (1992) compared the contribution of different gravity wave sources (specifically topography, convection, frontal systems and jet stream) on the momentum budget of the middle atmosphere and concluded that convectively generated waves played a significant role though their influence is not as much as topographically generated waves.

The experimental results from this study suggest that, in the absence of a background mean flow, the horizontal scale of thunderstorm-generated waves is set by the horizontal scale of the top of the clouds in a well-developed storm. Thus, the horizontal scale could be between 5 and 100 km. However, even though the oscillations of updrafts and downdrafts within a storm are responsible for generating the waves and have broad frequency spectra, their dominant frequency does not necessarily correspond to the dominant frequency of the waves generated. We find that the frequency of waves generated via the mechanical oscillator mechanism lies in a narrow range relative to the local buoyancy frequency, N. The wave frequency may range between $0.45N$ and $0.85N$, where N lies between 10^{-2} and 10^{-3} s^{-1}. The experiments show that the vertical displacement amplitudes of waves generated via the mechanical oscillator effect depends upon the distance updrafts overshoot their neutral buoyancy level and not upon the vertical scale of the whole storm as in the deep heating effect. From the experimental results, the vertical displacement amplitudes may range between 1 % and 5 % of the overshooting distance. Based upon observational studies this is about 30–150 m. The experiments also reveal that the average energy flux of thunderstorm-generated waves could be as large as 10^{13} erg s^{-1} based upon the rough estimates of energy flux in a single storm cell.

6. Conclusions

In this study, we have presented the results obtained when axisymmetric internal gravity waves are generated by turbulent buoyant plumes.

The results show that the radial wavelength of the waves is not set by the width of the plume at the density interface. Rather, the characteristic radial wavenumber is set by the mean radius of the plume cap. Even though the large-scale fluctuations at the top of the plume were quasi-regular with some identifiable characteristic peaks in their spectra, these frequency peaks did not match the observed frequency of the waves. Instead, the frequency of the waves relative to the buoyancy frequency was found to lie in a narrow frequency range $\sim 0.7N$. The vertical displacement amplitude of the waves shows a strong dependence on the maximum penetration of the plume beyond its neutral buoyancy level for the experiments considered.

The principal goal was to determine the percentage of the energy of the plume at the neutral buoyancy level that is extracted by the upward-propagating waves. We found that, on average, 4 % of the plume energy is realized as the energy of the

waves. Compared with the energy of a single storm cell we estimate the energy flux to be 10^{13} erg s^{-1}.

This research was supported by the Canadian Foundation for Climate and Atmospheric Science (CFCAS) GR-615.

Appendix. Average energy flux of waves

For a bounded domain of radius R, the energy flux over any circular area is given by

$$F_E = \int_0^{2\pi} \int_0^R (wp) r \,\mathrm{d}r \,\mathrm{d}\theta = 2\pi \int_0^R (wp) r \,\mathrm{d}r, \tag{A 1}$$

since both the vertical velocity w and the perturbation pressure p are independent of the radial coordinate θ for axisymmetric waves. Because the waves are assumed axisymmetric, we compute the average energy flux using Bessel series and define

$$w = \sum_n \sum_m \frac{1}{2} W_{nm} J_0(k_n r) \mathrm{e}^{\mathrm{i}(k_z z - \omega_m t)} + cc, \tag{A 2}$$

$$p = \sum_n \sum_m \frac{1}{2} P_{nm} J_0(k_n r) \mathrm{e}^{\mathrm{i}(k_z z - \omega_m t)} + cc, \tag{A 3}$$

where J_0 is the Bessel function of the first kind and order zero, W_{nm} and P_{nm} are the amplitudes of the w and p fields, k_z and ω_m are the vertical wavenumber and frequencies, respectively.

Substituting (A 2) and (A 3) into (A 1) and applying the orthogonality property of Bessel functions, we get

$$F_E = 2\pi \sum_n \sum_m P_{nm} W_{nm} \cos^2(k_z z - \omega_m t) \int_0^R [J_0(\alpha_n r/R)]^2 r \,\mathrm{d}r. \tag{A 4}$$

Using the properties of Bessel functions, this simplifies to

$$F_E = \pi R^2 \sum_n \sum_m P_{nm} W_{nm} \cos^2(k_z z - \omega_m t) J_1^2(\alpha_n), \tag{A 5}$$

where J_1 is the Bessel function of the first kind and order one.

The polarization relations of linear wave theory for each n and m gives

$$P_{nm} W_{nm} = \frac{\rho_0 N^3 \cos \Theta_m \sin 2\Theta_m}{2k_n} |A_{\xi nm}|^2,$$

where $k_n = \alpha_n / R$, Θ_m are the angles of propagation of each wave beam about the vertical and $A_{\xi nm}$ are the vertical displacement amplitudes. Equation (A 5) becomes

$$F_E = \frac{1}{2} \pi R^2 \rho_0 N^3 \sum_n \sum_m \cos \Theta_m \sin 2\Theta_m \cos^2(k_z z - \omega_m t) \frac{|A_{\xi nm}|^2 J_1^2(\alpha_n)}{k_n}. \tag{A 6}$$

Averaging over one wave period we get (2.19):

$$F_{wave} = \frac{1}{4} \pi R^2 \rho_0 N^3 \sum_n \sum_m \cos \Theta_m \sin 2\Theta_m \frac{|A_{\xi nm}|^2 J_1^2(\alpha_n)}{k_n}. \tag{A 7}$$

REFERENCES

Abraham, G. 1963 Jet diffusion in stagnant ambient fluid. *Tech. Rep*. 29. Delft Hydraulics Lab.

Alexander, M. J. & Barnet, C. 2007 Using satellite observations to constrain parameterizations of gravity wave effects for global models. *J. Atmos. Sci.* **64**, 1652–1665.

Alexander, M. J. & Pfister, L. 1995 Gravity wave momentum flux in the lower stratosphere over convection. *Geophys. Res. Lett*. **22**, 2029–2032.

Ansong, J. K., Kyba, P. & Sutherland, B. R. 2008 Fountains impinging on a density interface. *J. Fluid Mech.* **595**, 115–139.

Balachandran, N. K. 1980 Gravity waves from thunderstorms. *Monthly Weather Rev.* **108**, 804–816.

Bloomfield, L. J. & Kerr, R. C. 1998 Turbulent fountains in a stratified fluid. *J. Fluid Mech.* **358**, 335–356.

Bloomfield, L. J. & Kerr, R. C. 2000 A theoretical model of a turbulent fountain. *J. Fluid Mech.* **424**, 197–216.

Cerasoli, C. P. 1978 Experiments on buoyant-parcel motion and the generation of internal gravity waves. *J. Fluid Mech.* **86**, 247–271.

Chen, J. C. 1980 Studies on gravitational spreading currents. PhD thesis, California Institute of Technology.

Chen, J. C. & Rodi, W. 1980 *Turbulent Buoyant Jets: A Review of Experimental Data*. Pergamon.

Clark, T. L., Hauf, T. & Kuettner, J. P. 1986 Convectively forced internal gravity waves: results from two-dimensional numerical experiments. *Quart. J. R. Meteor. Soc.* **112**, 899–925.

Curry, M. J. & Murty, R. C. 1974 Thunderstorm-generated gravity waves. *J. Atmos. Sci.* **31**, 1402–1408.

Decamp, S., Kozack, C. & Sutherland, B. R. 2008 Three-dimensional schlieren measurements using inverse tomography. *Expts. Fluids* **44** (5), 747–758.

Dewan, E. M. & Coauthors 1998 MSX satellite observations of thunderstorm-generated gravity waves in mid-wave infrared images of the upper stratosphere. *Geophys. Res. Lett*. **25**, 939–946.

Didden, N. & Maxworthy, T. 1982 The viscous spreading of plane and axisymmetric gravity currents. *J. Fluid Mech.* **121**, 27–42.

Dohan, K. & Sutherland, B. R. 2003 Internal waves generated from a turbulent mixed region. *Phys. Fluids* **15**, 488–498.

Dohan, K. & Sutherland, B. R. 2005 Numerical and laboratory generation of internal waves from turbulence. *Dyn. Atmos. Oceans* **40**, 43–56.

Dunkerton, T. 1997 The role of gravity waves in the quasi-biennial oscillation. *J. Geophys. Res.* **102**, 26053–26076.

Fischer, H. B., List, E. J., Imberger, J. S. & Brooks, N. H. 1979 *Mixing in Inland and Coastal Waters*. Academic Press.

Flynn, M. R., Onu, K. & Sutherland, B. R. 2003 Internal wave excitation by a vertically oscillating sphere. *J. Fluid Mech.* **494**, 65–93.

Fovell, R., Durran, D. & Holton, J. R. 1992 Numerical simulations of convectively generated stratospheric gravity waves. *J. Atmos. Sci.* **49**, 1427–1442.

Fritts, D. C. & Alexander, M. J. 2003 Gravity wave dynamics and effects in the middle atmosphere. *Rev. Geophys.* **41** (1), 3.1–3.64.

Fritts, D. C. & Nastrom, G. D. 1992 Sources of mesoscale variability of gravity waves. II. Frontal, convective, and jet stream excitation. *J. Atmos. Sci.* **49**, 111–127.

Gedzelman, S. D. 1983 Short-period atmospheric gravity waves. *Monthly Weather Rev.* **111** (6), 1293–1299.

Grachev, A. I., Danilov, S. D., Kulichkov, S. N. & Svertilov, A. I. 1995 Main characteristics of internal gravity waves from convective storms in the lower troposphere. *Atmos. Oceanic Phys.* **30** (6), 725–733.

Holton, J. R. & Lindzen, R. S. 1972 An updated theory for the quasi-biennial cycle of the tropical stratosphere. *J. Atmos. Sci.* **29**, 1076–1080.

Ivey, G. N. & Blake, S. 1985 Axisymmetric withdrawal and inflow in a density-stratified container. *J. Fluid Mech.* **161**, 115–137.

Karoly, D. J., Roff, G. L. & Reeder, M. J. 1996 Gravity wave activity associated with tropical convection detected in TOGA COARE sounding data. *Geophys. Res. Lett*. **23** (3), 261–264.

Kaye, N. B. 2008 Turbulent plumes in stratified environments: a review of recent work. *Atmos. Ocean* **46** (4), 433–441.

Kotsovinos, N. E. 2000 Axisymmetric submerged intrusion in stratified fluid. *J. Hydraulic Engng, ASCE* **126**, 446–456.

Kumar, K. K. 2007 VHF radar investigations on the role of mechanical oscillator effect in exciting convectively generated gravity waves. *Geophys. Res. Lett*. L01803, doi:10.1029/2006GL027404, **34**.

Lane, T. P. 2008 The vortical response to penetrative convection and the associated gravity-wave generation. *Atmos. Sci. Let*. **9**, 103–110.

Lane, T. P., Reeder, M. J. & Clark, T. L. 2001 Numerical modelling of gravity wave generation by deep tropical convection. *J. Atmos. Sci.* **58**, 1249–1274.

Lane, T. P. & Sharman, R. D. 2006 Gravity wave breaking, secondary wave generation, and mixing above deep convection in a three-dimensional cloud model. *Geophys. Res. Lett*. L23813, doi:10.1029/2006GL027988, **33**.

Larsen, M. F., Swartz, W. E. & Woodman, R. F. 1982 Gravity–wave generation by thunderstorms observed with a vertically-pointing 430 MHz radar. *Geophys. Res. Lett*. **9** (5), 571–574.

Lee, J. H. W. & Chu, V. H. 2003 *Turbulent Buoyant Jets and Plumes: A Langrangian Approach*. Kluwer.

Lemkert, C. J. & Imberger, J. 1993 Axisymmetric intrusive gravity currents in linearly stratified fluids. *J. Hydraulic Engng, ASCE* **119** (6), 662–679.

Lindzen, R. S. & Holton, J. R. 1968 A theory of the quasi-biennial oscillation. *J. Atmos. Sci.* **25**, 1095–1107.

List, E. J. 1982 Mechanics of turbulent buoyant jets and plumes. In *Turbulent Buoyant Jets and Plumes*. (ed. W. Rodi), 1–68. Pergamon.

Lister, J. R. & Kerr, R. C. 1989 The propagation of two-dimensional and axisymmetric gravity currents at a fluid interface. *J. Fluid Mech.* **203**, 215–249.

Lu, D., VanZandt, T. E. & Clark, W. L. 1984 VHF Doppler radar observations of buoyancy waves associated with thunderstorms. *J. Atmos. Sci.* **41** (2), 272–282.

McDougall, T. J. 1981 Negatively buoyant vertical jets. *Tellus* **33**, 313–320.

McLandress, C. 1998 On the importance of gravity waves in the middle atmosphere and their parameterization in the general circulation models. *J. Atmos. Sol.-Terr. Phys.* **60**, 1357–1383.

McLaren, T. I., Pierce, A. D., Fohl, T. & Murphy, B. L. 1973 An investigation of internal gravity waves generated by a buoyantly rising fluid in a stratified medium. *J. Fluid Mech.* **57**, 229–241.

MEDOC Group 1970 Observations of formation of deep water in the Mediterranean. *Nature* **277**, 1037–1040.

Michaelian, M. E., Maxworthy, T. & Redekopp, L. G. 2002 The coupling between turbulent, penetrative convection and internal waves. *Euro. J. Mech.* B. *Fluids* **21**, 1–28.

Morton, B. R. 1959 Forced plumes. *J. Fluid Mech.* **5**, 151–163.

Morton, B. R. 1971 The choice of conservation equations for plume models. *J. Geophys. Res.* **76** (30), 7409–7416.

Morton, B. R., Taylor, G. & Turner, J. S. 1956 Turbulent gravitational convection from maintained and instantaneous sources. *Proc. R. Soc.* A **234**, 1–23.

Moustaoui, M., Joseph, B. & Teitelbaum, H. 2004 Mixing layer formation near the tropopause due to gravity wave–critical level interactions in a cloud-resolving model. *J. Atmos. Sci.* **61** (24), 3112–3124.

Mowbray, D. E. & Rarity, B. S. H. 1967 A theoretical and experimental investigation of the phase configuration of internal waves of small amplitude in a density stratified liquid. *J. Fluid Mech.* **28**, 1–16.

Onu, K., Flynn, M. R. & Sutherland, B. R. 2003 Schlieren measurement of axisymmetric internal wave amplitudes. *Expts. Fluids* **35**, 24–31.

Oster, G. 1965 Density gradients. *Sci. Am.* **213**, 70.

Paluszkiewcz, T. & Garwood, R. W. 1994 Deep convective plumes in the ocean. *Oceanography* **7**, 37–44.

Pandya, R. E. & Alexander, M. J. 1999 Linear stratospheric gravity waves above convective thermal forcing. *J. Atmos. Sci.* **56**, 2434–2446.

Papanicolaou, P. N. & List, E. J. 1988 Investigations of round vertical turbulent buoyant jets. *J. Fluid Mech.* **195**, 341–391.

Pfister, L., Chan, K. R., Bui, T. P., Bowen, S., Legg, M., Gary, B., Kelly, K., Proffitt, M. & Starr, W. 1993*a* Gravity waves generated by a tropical cyclone during the step tropical field program: a case study. *J. Geophys. Res.* **98** (D5), 8611–8638.

Pfister, L., Scott, S. & Loewenstein, M. 1993*b* Mesoscale disturbances in the tropical stratosphere excited by convection: observations and effects on the stratospheric momentum budget. *J. Atmos. Sci.* **50** (8), 1058–1075.

Pierce, A. D. & Coroniti, S. C. 1966 A mechanism for the generation of acoustic-gravity waves during thunderstorm formation. *Nature* **210**, 1209–1210.

Priestley, C. H. B. & Ball, F. K. 1955 Continuous convection from an isolated source of heat. *Quart. J. R. Meteorol. Soc.* **81** (384), 144–156.

Schott, F., Visbeck, M. & Fischer, J. 1993 Observations of vertical currents and convection in the Central Greenland Sea during the winter of 1988/89. *J. Geophys. Res.* **98**, 14401–14421.

Send, U. & Marshall, J. 1995 Integral effects of deep convection. *J. Phys. Oceanogr.* **25**, 855–872.

Song, I.-S., Chun, H.-Y. & Lane, T. P. 2003 Generation mechanisms of convectively forced internal gravity waves and their propagation to the stratosphere. *J. Atmos. Sci.* **60**, 1960–1980.

Stull, R. B. 1976 Internal gravity waves generated by penetrative convection. *J. Atmos. Sci.* **33**, 1279–1286.

Sutherland, B. R., Dalziel, S. B., Hughes, G. O. & Linden, P. F. 1999 Visualization and measurement of internal waves by 'synthetic schlieren'. Part 1. Vertically oscillating cylinder. *J. Fluid Mech.* **390**, 93–126.

Sutherland, B. R., Flynn, M. R. & Dohan, K. 2004 Internal wave excitation from a collapsing mixed region. *Deep Sea Res.* II **51**, 2889–2904.

Sutherland, B. R. & Linden, P. F. 2002 Internal wave excitation by a vertically oscillating elliptical cylinder. *Phys. Fluids* **14**, 721–731.

Townsend, A. A. 1964 Natural convection in water over an ice surface. *Quart. J. R. Meteorol. Soc.* **90**, 248–259.

Townsend, A. A. 1965 Excitation of internal waves by a turbulent boundary layer. *J. Fluid Mech.* **22**, 241–252.

Townsend, A. A. 1966 Internal waves produced by a convective layer. *J. Fluid Mech.* **24**, 307–319.

Tsuda, T., Murayama, Y., Wiryosumarto, H., Harijono, S. W. B. & Kato, S. 1994 Radiosonde observations of equatorial atmosphere dynamics over Indonesia. 2. Characteristics of gravity waves. *J. Geophys. Res.* **99** (D5), 10507–10516.

Turner, J. S. 1966 Jets and plumes with negative or reversing buoyancy. *J. Fluid Mech.* **26**, 779–792.

Turner, J. S. 1972 On the energy deficiency in self-preserving convective flows. *J. Fluid Mech.* **53**, 217–226.

Turner, J. S. 1973 *Buoyancy Effects in Fluids*. Cambridge University Press.

Vincent, R. A. & Alexander, M. J. 2000 Gravity waves in the tropical lower stratosphere: an observational study of seasonal and interannual variability. *J. Geophys. Res.* **105** (D14), 17971–17982.

Wang, P. K. 2004 A cloud model interpretation of jumping cirrus above storm top. *Geophys. Res. Lett.* L18106, doi:10.1029/2004GL020787, **31**.

Zatsepin, A. G. & Shapiro, G. I. 1982 A study of axisymmetric intrusions in a stratified fluid. *Izvestiya, Atmos. Ocean Phys.* **18**, 77–80.